Influence of the Atlantic Multidecadal Variability on the climate response to external forcing

by

Sarah Hyatt

A thesis
presented to the University of Waterloo
in fulfillment of the
thesis requirement for the degree of
Master of Mathematics
in
Applied Mathematics

Waterloo, Ontario, Canada, 2018

I hereby declare that I am the sole author of this thesis. This is a true copy of the thesis, including any required final revisions, as accepted by my examiners.

I understand that my thesis may be made electronically available to the public.

Abstract

Internal climate variability has been found to influence the climate response to an external forcing such as CO_2. This thesis investigates the influence of the Atlantic Multidecadal Variability (AMV), a mode of internal climate variability in the North Atlantic Ocean, on the response to external forcing. The AMV is a 60 - 80 year fluctuation in the sea surface temperatures of the North Atlantic that has widespread effects on climate. Using simulations run on an ocean-atmosphere general circulation model (GCM), it is found that the AMV phase significantly impacts the regional response to CO_2: in the extratropical Northern Hemisphere, Eurasia warms more, and North America and the North Pacific warm less, in the warm phase of the AMV. The mechanisms of the AMV-related response are explored using a constructed circulation analog method. Changes in teleconnections between the tropical and extratropical Pacific contribute to the dynamical component of the difference in response to forcing between AMV phases, while differences in sea ice may contribute to the thermodynamic component. Interestingly, some aspects of the AMV-related response are robust with different external forcings. Finally, using simulations run on an atmospheric GCM, the role of sea ice in forcing atmospheric AMV-related anomalies is investigated. It is found that sea ice in the Barents and Greenland Seas plays a large role in forcing local temperature anomalies.

Acknowledgements

I would like to thank my supervisor, Chris Fletcher, for his guidance and support throughout this research project.

Dedication

This thesis is dedicated to my mom and dad, for always encouraging me.

Table of Contents

List of Figures

List of Tables

Abbreviations

AGCM Atmospheric general circulation model

AMOC Atlantic Meridional Overturning Circulation

AMV Atlantic Multidecadal Variability

AO Arctic Oscillation

CESM Community Earth System Model

CMIP Coupled Model Intercomparison Project

CNRM Centre National de Recherches Météorologiques

DJF December January February

GCM General circulation model

JJA June July August

MAM March April May

NCAR CAM4 National Center for Atmospheric Research Community Atmosphere Model 4

PICTL Pre-industrial control

PR Precipitation

PSL Sea level pressure

SIC Sea ice concentration

SNC Snow cover

SON September October November

SST Sea surface temperature

TAS Near-surface air temperature

Chapter 1

Introduction

1.1 Decadal variability in the North Atlantic

Currently, two of the largest challenges in atmosphere-ocean science are seasonal-to-decadal climate prediction (Meehl et al, 2014; Cassou et al, 2018), and understanding and attributing anthropogenic climate change, particularly on regional scales (Stocker and Coauthors, 2013). The presence of large internal climate variability, occurring on many different timescales, adds to the difficulty of both of these challenges (Hawkins and Sutton, 2009). Aspects of these challenges, related to decadal predictability and to the understanding of anthropogenic and internal climate variability on decadal timescales, are relevant here.

Regarding the first challenge, the particular interest here is on decadal prediction and predictability. Decadal prediction is a relatively new field, emerging around a decade ago (Meehl et al, 2009), which involves the near-term climate (one to three decades into the future). Predictions of this time period are very relevant for climate change related policy and adaptation. Decadal predictions were part of the fifth Coupled Model Intercomparison Project (CMIP5) (Taylor et al, 2012), and more projects involving decadal prediction are underway (eg. Boer et al, 2016). Decadal predictions attempt to improve the skill of climate predictions by initializing from the observed climate. In the long term, the chaotic nature of the climate system will erase the impact of the initial conditions (Lorenz, 1975). The question of for how long the initial conditions will have a discernible influence on the predicted climate, and therefore provide addition skill to the prediction, is complex, and an active area of investigation (Meehl et al, 2014 and references within).

The second challenge, more specifically, is that internal variability and anthropogenic influences both contribute to climate changes. This complicates the understanding and at-

tribution of anthropogenic climate change, particularly on regional scales and over shorter time periods, in which cases the influence of internal variability is most relevant (Hawkins and Sutton, 2009). First, internal variability on various timescales can amplify or counteract the regional climate response to anthropogenic influences: for example, decadal internal variability contributed to an apparent slowdown in global warming in the early 2000s (eg. Watanabe et al, 2014). Second, in addition to directly influencing the climate, internal variability can influence the climate response to anthropogenic influences: for example, it has recently been shown that two long term modes of internal variability, the Pacific Decadal Oscillation and the Atlantic Multidecadal Variability (AMV, which is of particular interest here), influence the climate response to sea ice loss due to greenhouse gas-induced warming (Screen and Francis, 2016; Osborne et al, 2017).

The North Atlantic is a particularly interesting region for decadal prediction and the influence of internal variability. This is in large part due to internal variability in this region which occurs on decadal to multidecadal timescales, specifically the AMV and the Atlantic Meridional Overturning Circulation (AMOC). The remainder of this section will present the current state of knowledge on climate predictability and variability, particularly in the North Atlantic region, in more detail.

1.1.1 Decadal variability and predictability

The atmosphere is unstable to small perturbations in the natural system as well as in state-of-the-art climate models (Lorenz, 1963). A distribution of climate model simulations which are initialized at nearly identical states will, eventually, be no more alike than a distribution initialized at entirely random states. This means there is a limit on the initial value predictability, defined as the time that a distribution of climate states from nearly identical initial values is distinct from a climatological distribution (eg. Branstator et al, 2012). This limit impacts both attempts to make accurate near-term climate predictions, as well as attempts to characterize the influence of a given initial state on some aspect of climate, as here.

Predictability comes from parts of the system which act on relatively longer timescales, or "behave more 'sluggishly' ", than other parts (Lorenz, 1975). The oceans, in particular, act on longer timescales than the atmosphere. This can be measured in sea surface temperature (SST) or, better, in the mixed layer integrated temperature, which is not majorly influenced by short-term weather fluctuations and yet may influence the atmosphere (eg. Branstator and Teng, 2010). (Other parts of the earth system with long time scales, such as sea ice, can also contribute predictability to the system.)

An equation that allows the predictability of a model to be estimated is presented by Palmer (2000). Assume a perfect deterministic climate model, with an instantaneous state of the climate system represented as X, and the N-dimensional conservation equations of the model expressed as

$$\dot{X} = F(X). \tag{1.1}$$

The uncertainty in the initial state at time t_0 which results from errors in the initial values can be represented by a probability density function, $\rho(X, t_0)$, so that the probability of the true initial state being within some volume V of phase space is

$$\int_V \rho(X, t_0) dV. \tag{1.2}$$

Palmer (2000) shows that the Liouville conservation equation describes the evolution of ρ:

$$\frac{\partial \rho}{\partial t} = -\frac{\partial}{\partial X}(\dot{X}\rho) \equiv L\rho. \tag{1.3}$$

Some level of predictability exists so long as $\rho(X, t)$ is distinct from the invariant distribution of the attractor. That is, predictability is lost when the forecast distribution is no longer distinguishable from the distribution associated with the set of states towards which the climate system, starting from any initial conditions, may evolve, because at this point no additional information is gained by knowing the initial state. However, practically, this equation is not easily solvable for realistic weather or climate predictions.

In practice, predictability is generally estimated using ensembles of predictions from climate models. Two rates are important for initial value predictability: the rates at which the spread and the ensemble mean of the initial value distribution approach climatological values (Branstator and Teng, 2010). These rates can be determined with climate modelling experiments, by comparing multiple simulations that vary only by small perturbations to the initial atmospheric conditions (eg. Collins and Allen, 2002; Branstator and Teng, 2010). The predictability determined from such experiments is an upper bound on the actual predictability of the model, as it is measured from completely identical initial ocean conditions whereas in practice, the initial ocean state will never be known exactly. Interestingly, Scaife and Smith (2018) recently found that the natural climate is, apparently ubiquitously, more predictable than the model climate, due to a too small signal-to-noise ratio in climate model output. Thus, the predictability calculated from models in this way is likely to underestimate the predictability in nature.

The timescale on which initial value predictability exists depends on numerous factors. First, it is highly model dependent - that is, it varies between different climate models

of similar complexity (i.e. all coupled atmosphere-ocean models), by up to a factor of 10 (Branstator et al, 2012). Note that due to the short observational record, the predictability of the natural system cannot be determined in a similar way to that of a climate model, and therefore the actual predictability in nature is not known.

Further, initial value predictability varies for different climate variables and different locations. As one might expect, internal ocean variables have long initial value predictability, on up to decadal timescales (Griffies and Bryan, 1997). Surface air temperature predictability is short (seasonal timescales) over land, but longer (interannual timescales) over the tropical oceans and longer still (decadal timescales) over the extratropical oceans (Collins, 2002). Other variables, such as precipitation, only have predictability on seasonal time scales (Collins, 2002). The specific initial values can also modify the predictability. More extreme initial values are associated with longer predictability than initial values that are close to the climatological mean (Griffies and Bryan, 1997; Collins et al, 2006).

The North Atlantic is, in most climate models, the region where there is the most potential for improved skill from specifying initial values (Meehl et al, 2014). In the North Atlantic, predictability has been found on decadal timescales. Specific lengths of predictability vary based on the factors listed above, but North Atlantic predictability been found to exist for up to two decades (Msadek et al, 2010). The decadal predictability in the North Atlantic is in part due to the strong multidecadal variability in this region, specifically the Atlantic Meridional Overturning Circulation (AMOC) and the Atlantic Multidecadal Variability. This multidecadal variability in the North Atlantic will be explored next.

1.1.2 Atlantic Multidecadal Variability

The Atlantic Multidecadal Variability (AMV) is an internal mode of variability in the North Atlantic Ocean (Kerr, 2000), and describes the dominant pattern of SST variability in this region. On timescales of approximately 60 - 80 years, the North Atlantic alternates between a warm phase ($AMV_{(+)}$) and a cold phase ($AMV_{(-)}$). The observed AMV timeseries and $AMV_{(+)}$ pattern are shown in Fig. 1.1. In $AMV_{(+)}$, virtually all of the North Atlantic basin has positive SST anomalies, and the largest anomalies occur in a horseshoe pattern extending throughout the tropical Atlantic, along the eastern side of the basin, and along the north of the basin into the Labrador Sea. The strongest anomalies are in the subpolar region. $AMV_{(-)}$ has a similar pattern, but with negative SST anomalies. Various different methods are used to define the AMV index, but they are generally a measure of the long term (i.e. low pass filtered) area-averaged SST anomalies in the North Atlantic basin, after

anthropogenically forced anomalies have been removed. For example, Enfield et al (2001) calculates the AMV index as the ten-year running mean of the detrended SST anomalies in the Atlantic north of the equator. Approximately 0.5 K separates the extremes of the sea surface temperatures (SSTs) in each phase (Alexander et al, 2014). Globally, Knight et al (2005) finds the global temperature to vary decadally with the strength of the thermohaline circulation (believed to be associated with the AMV), with a 0.1 K difference in global mean temperature between circulation extremes. Comparing these values to the Paris Agreement goals of 1.5 K or at most 2 K of global mean warming (UNFCCC, 2015), the AMV-related decadal changes in temperature are not insignificant.

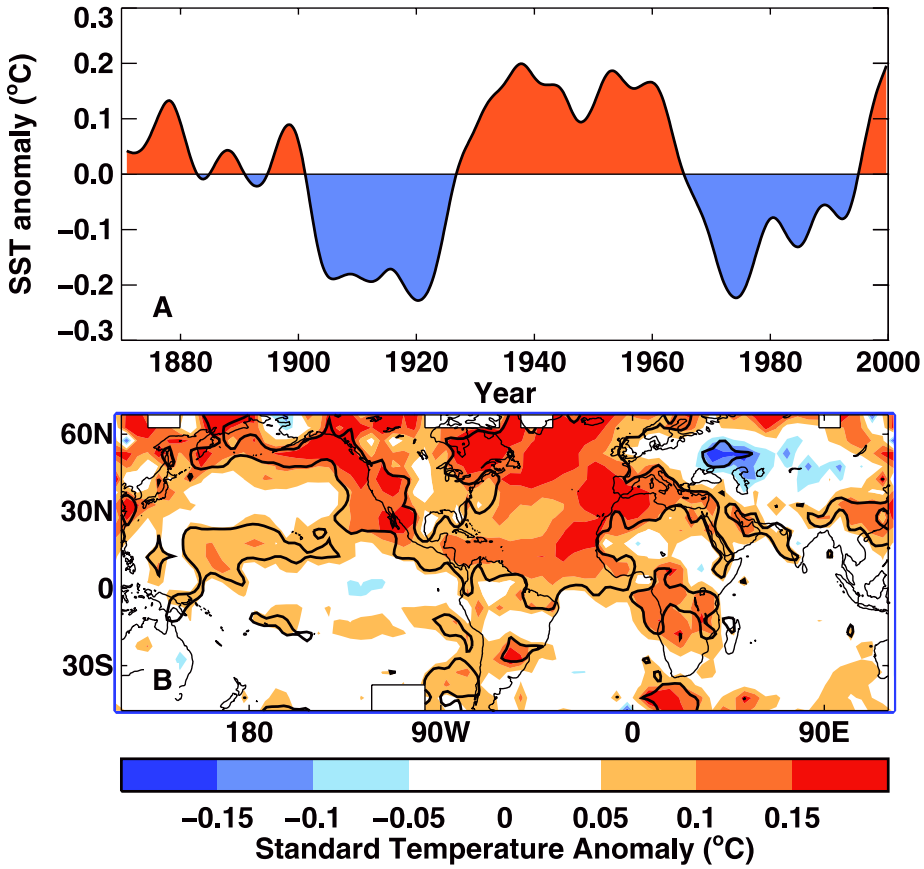

Figure 1.1: (Top) AMV index and (bottom) $AMV_{(+)}$ pattern represented as the anomaly in surface temperature associated with one positive standard deviation of the AMV index. Both are based on observations/reanalysis data. From Knight et al (2005).

The AMV has numerous widespread effects on climate. The AMV phase has been

found to be connected with African Sahel droughts (Folland et al, 1986); monsoons in India (Zhang and Delworth, 2006) and East Asia (Lu et al, 2006); Atlantic hurricanes (Knight et al, 2006); North American and European midlatitude climates (Sutton and Hodson, 2005; Baines and Folland, 2007). The AMV index is also correlated with Arctic temperature anomalies (Chylek et al, 2009) and Arctic sea ice fluctuations (Miles et al, 2014).

The mechanism causing the AMV remains a subject of some debate. The long-held prevailing theory (Bjerknes, 1964; Delworth and Mann, 2000; Zhang and Wang, 2013) has been that the AMV is a function of the strength of the Atlantic Meridional Overturning Circulation (AMOC). The AMOC is a large-scale overturning circulation in the Atlantic; the stronger upper cell, occurring in the North Atlantic, consists of warm salty water flowing northwards in the upper layers (approximately the upper 1 km) of the North Atlantic, cooling and freshening of this water at high latitudes, and cold water flowing south at depth and eventually upwelling. The AMOC therefore has a large role in ocean heat transport in the North Atlantic, hence the hypothesis that it influences the AMV. Specifically, a stronger AMOC is believed to lead to a warm AMV phase through anomalous northward heat transport, while a weaker AMOC leads to a cold AMV phase.

Observations (eg. Gulev et al, 2013) and modelling experiments (eg. Zhang and Wang, 2013; Ba et al, 2013) have provided evidence for this theory. Gulev et al (2013) shows that, on decadal timescales in the North Atlantic, the ocean drives the surface turbulent heat fluxes to the atmosphere, consistent with the AMV being driven by ocean dynamics. Zhang and Wang (2013) find that, in most of the 18 CMIP5 models considered, the relationship between AMOC and AMV, examined through lead-lag correlations, is consistent with a stronger (weaker) AMOC leading to a warm (cold) AMV phase, which then leads to a weakening (strengthening) of the AMOC. However, observational evidence is scarce, as less than 15 years of continuous, direct measurements of the AMOC are available (Clement et al, 2015), and evidence from modelling studies is inconclusive, in part because results are model dependent (Zhang and Wang, 2013). More recently, a theory has been put forward that the AMV is at least partially driven by atmospheric forcing (eg. Clement et al, 2015; Bellomo et al, 2018). Some climate models appear to have an AMV in the absence of ocean dynamics (eg. Clement et al, 2015), and historical forcing has been found to have a role in driving the AMV (Murphy et al, 2017; Bellomo et al, 2018). Overall, it is likely that both ocean dynamics, such as the AMOC, and atmospheric forcing influence the AMV.

1.1.3 Dynamics of the AMOC

Having established that the AMOC is likely at least part of the mechanism driving the AMV, we now briefly explore its dynamics. Large-scale overturning flow, such as that in the AMOC, can be well described by the planetary geostrophic equations. These equations and the shallow water equations will be used in this section; both sets of equations are discussed next, following the derivations in Vallis (2006).

The shallow water equations describe a vertically thin layer of fluid with constant density. These equations use the hydrostatic approximation

$$\frac{\partial p}{\partial z} = -\rho g, \tag{1.4}$$

where p is pressure, ρ is density, and g is acceleration due to gravity. That is, in the vertical, the pressure force is balanced by the gravitational force. This approximation is well satisfied in the shallow water case, due to the small ratio between the vertical and horizontal scales. For a single shallow layer of total thickness h, with a free upper surface at height η, the horizontal momentum equation and the mass continuity equation are

$$\frac{D\mathbf{u}}{Dt} + \mathbf{f} \times \mathbf{u} = -g\nabla\eta, \tag{1.5}$$

$$\frac{Dh}{Dt} + h\nabla \cdot \mathbf{u} = 0, \tag{1.6}$$

where $\mathbf{u}$ is the horizontal velocity, and $\mathbf{f} = f\mathbf{k}$ where f is the Coriolis parameter.

The planetary geostrophic equations can be derived from the primitive equations by making several assumptions. First, it is assumed that the Rossby number, Ro, is small, where Ro is the ratio of the magnitudes of the advective and Coriolis terms, so small Ro indicates that rotation effects are important. Thus, geostrophic balance is assumed - i.e., the Coriolis force is balanced by the pressure force. It is also assumed that the scale of motion, L, is much larger than the deformation scale, L_d, such that

$$F = (L/L_d)^2 \gg 1, \tag{1.7}$$

and the relationship between Ro and F is

$$FRo = \mathcal{O}(1). \tag{1.8}$$

Finally, it is assumed that time scales advectively. The primitive equations are themselves derived from the Navier-Stokes equations, and require the hydrostatic approximation.

However, the planetary geostrophic equations are quite complex, and they cannot be nicely simplified in a way that allows us to better understand MOC dynamics (Vallis, 2006). Many approximate models have been created to attempt to describe MOC physics in a simple yet useful way. One such idealized model is the shallow water Stommel-Arons type model. The following description is based on that presented in Vallis (2006). This model attempts to provide a conceptual description of oceanic abyssal flow. The structure of the model, shown in Fig. 1.2 is simple. The deep ocean is represented by a single layer of moving fluid on a sector of a rotating sphere. Above the deep ocean, there is another layer of fluid which is stationary. The deep ocean has a localized mass source at the pole, and a uniform mass sink everywhere else. The mass source is analogous to convection (i.e. the cold, salty water which sinks at high latitudes) while the mass sink is analogous to diffusive upwelling into the upper layer of the ocean. The sink and source are specified to be equal and opposite in magnitude, so that there is no net mass flux in the deep ocean. The model requires approximations that are not true in the real ocean: the upwelling is assumed to be uniform, and the ocean is assumed to be flat-bottomed.

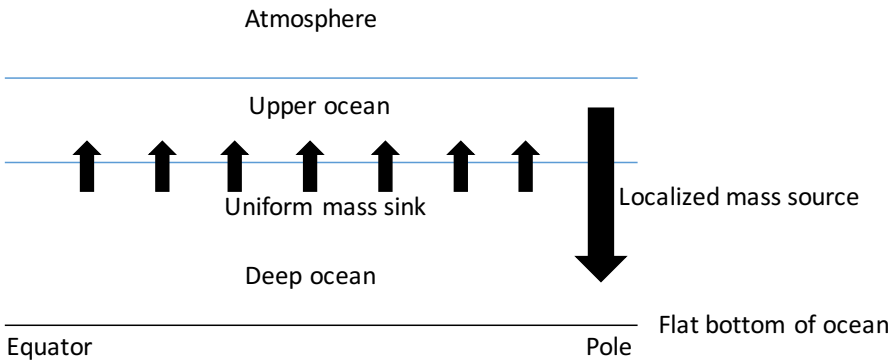

Figure 1.2: Diagram of shallow water Stommel Arons model described in text. This is based on a similar diagram in Vallis (2006).

The planetary geostrophic reduced-gravity shallow water equations then describe the motion in the deep ocean:

$$-fv = -g'\frac{\partial h}{\partial x} - ru, \tag{1.9}$$

$$fu = -g'\frac{\partial h}{\partial y} - rv, \tag{1.10}$$

$$\frac{\partial h}{\partial t} + \nabla \cdot (\mathbf{u}h) = S. \tag{1.11}$$

Here, f is the Coriolis parameter, $\mathbf{u} = (u, v)$ is two-dimensional velocity, g' is the reduced gravity, h is the height of the deep ocean layer, r is a constant frictional coefficient, and S is the mass source term. The reduced gravity is defined as

$$g' = \frac{g(\rho_2 - \rho_1)}{\rho_1}, \tag{1.12}$$

where g is the acceleration due to gravity, ρ_1 is the density of the upper layer, and ρ_2 is the density of the lower layer.

These equations can be written in terms of mass transport instead of velocity. In a region away from the convective mass source, the equations are then:

$$-fV = -\frac{\partial \Phi}{\partial x} - rU, \tag{1.13}$$

$$fU = -\frac{\partial \Phi}{\partial y} - rV, \tag{1.14}$$

$$\nabla \cdot \mathbf{U} = S_u, \tag{1.15}$$

where S_u is the component of the mass source term representing upwelling,

$$\mathbf{U} = U\mathbf{i} + V\mathbf{j} = uh\mathbf{i} + vh\mathbf{j}, \tag{1.16}$$

and

$$\Phi = \frac{g'h^2}{2}. \tag{1.17}$$

Manipulation of these equations gives

$$\frac{\beta}{f}\frac{\partial \Phi}{\partial x} = -fS_u - f\nabla \cdot (\frac{r}{f^2}\nabla \Phi). \tag{1.18}$$

Where effects of friction are small, the third term is negligible. Thus, by dominant balance the equation is

$$\beta V = -fS, \tag{1.19}$$

indicating poleward flow. Clearly, however, poleward flow everywhere does not make sense as it would violate mass conservation laws. Instead, to compensate for the interior poleward flow, a frictional western boundary current is expected.

The assumption of a western boundary is justified based on vorticity dynamics. The potential vorticity equation is

$$\frac{D}{Dt}\frac{f}{h} = -\frac{fS_u}{h^2} + \frac{1}{h}\text{curl}_z\mathbf{F}, \tag{1.20}$$

where $\mathbf{F}$ is friction. Flow from the source at the northern boundary moves towards smaller h along the boundary layer. The left hand side of the vorticity equation is therefore negative, and (as S_u is negative) must be balanced by a negative $\text{curl}_z\mathbf{F}$; that is, the friction must contribute negative vorticity to the flow. Friction counters motion, so the total vorticity of the flow must be positive, meaning the flow is counterclockwise. Counterclockwise flow from the northern source must flow southwards along a western boundary, as assumed.

Now, let

$$\Phi = \Phi_I + \Phi_B, \tag{1.21}$$

where the components are the interior and boundary fields respectively. For the interior field, friction is small, so the third term of 1.18 is negligible. For the boundary field, the friction is larger and the dominant balance is between the first and third terms of 1.18, giving the equation

$$\beta\frac{\partial\Phi_b}{\partial x} = -r\frac{\partial^2\Phi_b}{\partial x^2}, \tag{1.22}$$

which has the solution

$$\Phi_b = P(y)\exp(-\beta x/r). \tag{1.23}$$

To determine $P(y)$, mass conservation must be used. There are three mass flux terms in the system which must sum to zero, as mass must be conserved. Specifically, at a given latitude y, the magnitude of the southward boundary flux must be equal to the magnitude of the northward interior flux minus the mass that has upwelled south of y. That is,

$$P(y) = \text{boundary flux} = -\text{interior flux} + \text{upwelling flux}. \tag{1.24}$$

The upwelling flux is simply area south of y multiplied by the uniform mass sink:

$$\text{upwelling flux} = S_u(x_E - 0)(y - 0) = S_u x_E y. \tag{1.25}$$

The interior poleward mass flux is the integral over all longitudes of the latitudinal mass transport at y:

$$\text{interior flux} = \int_0^{x_E} V\,dx, \tag{1.26}$$

which evaluates to

$$\text{interior flux} = -\frac{f}{\beta} S x_E. \tag{1.27}$$

Thus, the boundary flux is

$$P(y) = S_u x_E y + \frac{f}{\beta} S x_E = 2 S_u x_E y \tag{1.28}$$

(by using $f = \beta y$).

These equations for the fluxes tell us several properties of the flow. As expected, it is polewards in the interior, and equatorwards at the boundary. At latitudes closer to the equator, the boundary flux is weaker; this shows that mass moves from the boundary into the interior as it travels southward. Finally, noting that $S_u x_E y_N = -S_0$ (i.e., that the mass source is equal and opposite to the total mass sink, as stated above), the boundary flux can be re-written

$$P(y) = -2 S_0 \frac{y}{y_N}, \tag{1.29}$$

where y_N is the latitude of the northern boundary; then it is clear to see that at y_N, the boundary mass flux is twice as large as the source. This is only possible if the flow recirculates. These properties of this simple model are, qualitatively, similar to the AMOC in nature.

Finally, the complete solution is

$$\Phi = \frac{f^2}{\beta} S_u (x_E - x) + 2 S_u X_E y \exp \frac{-\beta x}{r}. \tag{1.30}$$

Overall, this is a very simplified model, the required assumptions limit its relevance to the real world, and the AMOC is in fact influenced by many more processes than are represented in the Stommel-Arons model, including winds, basin geometry and bottom topography, advection, and smaller scale processes (Schloesser et al, 2012). However, this model gives a broad conceptual picture of some of the dynamics behind the AMOC, and thus the AMV. In particular, we can gain useful insight into heat transport in the North Atlantic. Recall that the mass source at the pole is analogous to cold, salty water sinking at high latitudes, which then flows south at depth along the western boundary. Clearly, then, a stronger AMOC has more flow of cold northern waters towards the equator, and thus more northward transport of warm water. This is generally consistent with actual

heat transport in the North Atlantic, which leads to the proposal that the AMV is due to fluctuations in AMOC strength, as increased heat transport into the North Atlantic would lead to warmer SSTs.

This model cannot answer the question of whether the AMOC strength in fact fluctuates, or of what physical mechanisms drive such changes. Indeed, the AMOC strength has been found to fluctuate on decadal timescales, and its variability is linked with the AMV (eg. Delworth and Mann, 2000; Knight et al, 2005). There is debate regarding the mechanism of decadal AMOC variability, although a recent review (Buckley and Marshall, 2016) suggests that the key mechanism is a response to buoyancy anomalies on the western boundary of the North Atlantic basin, along the boundary between the subtropical and subpolar gyres.

Overall, the dynamics of the AMOC are complex and still not entirely understood. Therefore, the mechanisms of the AMV are also still a matter of debate. However, as presented above, there is strong evidence that decadal fluctuations in the AMOC are at least partially responsible for the AMV.

1.2 Teleconnections

The AMV, as mentioned in the previous section, has impacts on climate across the globe. While some of these appear to have direct, thermodynamic mechanisms, others do not. The AMV can exert influences on climate in remote regions through teleconnections. Teleconnections are connections between changes in weather that occur in regions that are distant from each other (AMS, 2012). Often, such a connection occurs through changes in large-scale pressure and wind. One example of a well-known teleconnection is the linked variations in sea level pressure over Darwin, Australia and Tahiti, termed the Southern Oscillation; this teleconnection is associated with variations in precipitation in the tropics and subtropics (Kousky et al, 1984).

As an example of AMV influence through teleconnections, it has been found (Lyu et al, 2017) that $\text{AMV}_{(+)}$ is associated with changes in the tropical Pacific climate: specifically, an anomalously cool Pacific Ocean, and a westward-shifted Walker circulation. The Walker circulation is a clockwise atmospheric circulation cell in the equatorial Pacific, with a rising branch in the western Pacific and a sinking branch in the eastern Pacific. These changes lead to anomalous descending motion in this region, which itself leads to the excitation of a stationary, northward-extending Rossby wave which is associated with climate changes in the North Pacific. In this thesis, the role of the AMV in climatological and externally

influenced teleconnections will be explored; thus, the theory behind such teleconnections is presented here.

Atmospheric Rossby waves are planetary scale waves which affect climate on large scales. Important properties of Rossby waves can be derived in a simplified model of the atmosphere. Consider one layer of a barotropic atmosphere. The mechanism of Rossby wave generation is through vorticity conservation, so the important equation here is the vorticity equation,

$$\frac{\partial \zeta}{\partial t} + \mathbf{v} \cdot \nabla \zeta = -\zeta D + F, \tag{1.31}$$

where ζ is absolute vorticity, $\mathbf{v}$ is horizontal wind velocity, $D = \frac{\partial u}{\partial x} + \frac{\partial v}{\partial y}$ is horizontal divergence, and F is the frictional term. (Although this is an approximation of the real atmosphere, Sardeshmukh and Hoskins (1985) find that it adequately describes the major large-scale vorticity dynamics in the tropics.)

Following Sardeshmukh and Hoskins (1988) and Shimizu and de Albuquerque Cavalcanti (2011), the velocity can be written as the sum of its rotational and divergent components, respectively:

$$\mathbf{v} = \mathbf{v}_{\mathbf{\Psi}} + \mathbf{v}_{\chi}. \tag{1.32}$$

Then, the vorticity equation 1.31 may be rewritten as

$$\frac{\partial \zeta}{\partial t} + \mathbf{v}_{\mathbf{\Psi}} \cdot \nabla \zeta = S + F = -\zeta D - \mathbf{v}_{\chi} \cdot \nabla \zeta + F. \tag{1.33}$$

The leftmost side of 1.33 contains all the rotation terms, which involve Rossby wave propagation. The right hand sides of 1.33 contain the Rossby wave forcing terms: a (negligible) frictional term and the Rossby wave source,

$$S = -\zeta D - \mathbf{v}_{\chi} \cdot \nabla \zeta. \tag{1.34}$$

The expression for the Rossby wave source tells us that Rossby wave forcing is larger when the absolute vorticity, divergence, the divergent velocity, and the gradient of vorticity are larger.

In the tropics, anomalously warm SSTs enhance the transfer of heat to the troposphere. The enhanced deep convection, as well as being connected to higher precipitation, leads to increasing divergence at high levels. Thus, Rossby waves are associated with heating and

precipitation anomalies in the tropics. However, near the equator, the gradient of vorticity is small: the planetary vorticity gradient at a latitude ϕ is given by

$$\beta = \frac{d}{dy}(2\Omega \sin\phi), \tag{1.35}$$

where Ω is the angular speed of the earth, and $\partial\phi = a\partial y$ where a is the radius of the earth. Very near the equator, then, the gradient of planetary vorticity is small since ϕ and thus $\sin\phi$ are small. Additionally, in the subtropics, there are strong vorticity gradients associated with the jet streams. Therefore, the Rossby wave source is largest not at the center of such tropical anomalies, but at their edges in the subtropics (Shimizu and de Albuquerque Cavalcanti, 2011).

Rossby waves generated in the tropics by such mechanisms can then propagate polewards; this is the means through which teleconnections occur.

1.3 Role of internal variability in the response to external forcing

Previous work has shown that the background climate state, controlled in part by internal variability, can modulate the climate response to an external forcing. The atmospheric circulation response to sea ice loss has been suggested to depend on the background state of sea ice (Semenov and Latif, 2015). Balmaseda et al (2010) find that the background state of the ocean and atmosphere influences the atmospheric response to sea ice loss; specifically, the polarity of the Arctic Oscillation-like response is influenced by the background SST. Additionally, it has been found that the Pacific Decadal Oscillation, a long term mode of variability, influences the climate response to sea ice loss (Screen and Francis, 2016).

Most relevantly, the AMV has been found to influence the response to external forcing (Osborne et al, 2017; Li et al, 2018; Vial et al, 2018). Osborne et al (2017) used an atmospheric general circulation model (AGCM) to compare the atmospheric response to sea ice loss with $\text{AMV}_{(+)}$ or $\text{AMV}_{(-)}$ SSTs, and found that the response in the North Pacific is sensitive to AMV phase. Li et al (2018) used both AGCM experiments and reanalysis data, and found that sea ice loss induces a different Arctic Oscillation response depending on the AMV phase. Finally, Vial et al (2018) find that the AMV influences the tropical precipitation and circulation response to external forcing, by changing the magnitude of the CO_2-forced weakening of the Walker Circulation.

1.4 Role of ocean-atmosphere coupling

There exists a hierarchy of complexities of climate models (Held, 2005). Atmosphere-ocean coupled general circulation models (GCMs) are among the most complex, using the Navier-Stokes equations as well as various parameterizations to simulate climate, including interactions between ocean and atmosphere. Atmospheric GCMs (AGCMs) are one step less complex, with a similarly simulated atmosphere that responds to, but cannot influence, the prescribed ocean and sea ice.

AGCMs have advantages: in addition to being less computationally expensive to run, they allow for experiments which isolate cause (i.e. boundary forcing) and effect (i.e. atmospheric circulation). This separation of cause and effect is very difficult to achieve in coupled models, and can be very useful for improving understanding of climate variability and change. However, experiments using prescribed boundary forcing inherently assume that oceanic and sea ice feedbacks, which are not present in AGCM simulations due to the lack of ocean-atmosphere coupling, are not important for understanding the primary details of the atmospheric response.

The effect of the lack of coupling in AGCMs on both internal variability and externally forced changes has been investigated; the latter is of interest here. He and Soden (2016a) compare externally forced climate changes in an AGCM and a GCM, and find that the response to forcing in the GCM can be well reproduced in the AGCM, justifying the use of AGCMs in simulating anthropogenic climate changes. Deser et al (2016a) find that the overall structure of the northern extratropical atmospheric circulation response to Arctic sea ice loss is the same with and without ocean-atmosphere coupling. However, with coupling, the response is magnified by roughly 50%. Consistently, Smith et al (2017) also find a magnified atmospheric response to sea ice loss with coupling. Further, Deser et al (2015) find that a lack of ocean-atmosphere coupling geographically confines the response to Arctic sea ice loss to the region north of 30°N, whereas with coupling there is a global response.

Overall, GCMs and AGCMs are both extremely useful tools in the correct situation: GCMs more accurately simulate the real climate, as they allow the ocean and atmosphere to interact, while AGCMs allow for more direct investigations of cause and effect. Thus, both types of model will be used here.

1.5 Objectives and research questions

Previous work has shown that the background climate state, controlled in part by internal variability, can modulate the climate response to an external forcing (Boé et al, 2010; Semenov and Latif, 2015; Balmaseda et al, 2010; Screen and Francis, 2016). In terms of climate prediction, this may be of particular interest in the North Atlantic, where the multi-decadal variability in the AMOC and AMV lead to especially long potential predictability. While previous studies have investigated the impact of North Atlantic variability, specifically the AMV, on the response to external forcing (Osborne et al, 2017; Li et al, 2018), none have done so using simulations with an atmosphere-ocean coupled model. Thus, the influence of the AMV on the climate response to external forcing in a coupled climate model is worthy of investigation.

The main objective of this thesis is to describe, and identify the mechanisms controlling, the AMV influence on the northern extratropical response to external forcing. The set of coupled model AMV initialization experiments allows for the investigation of the influence of the AMV, including its potential mechanisms and its dependence on the applied external forcing.

However, while atmosphere-ocean coupling can improve the accuracy of the response to forcing, it is very difficult to separate cause and effect in output from a coupled climate model. Using the coupled model experiments, it is therefore difficult to identify with certainty the mechanisms which cause the AMV influence on the climate response. A second set of simulations using an uncoupled climate model is developed to isolate the influence of AMV-related sea ice anomalies on the atmosphere.

Chapter 2

Data and methods

The first section of this chapter describes the two sets of modelling experiments which will be discussed in this thesis. First, the AMV initialization experiments and the coupled model on which they were run, CNRM-CM5, are described. This set of experiments was designed to investigate the influence of the AMV phase on the response to external forcing in a coupled model. The results of these experiments will be presented in Chapter 3. Second, the sea ice forcing experiments and the AGCM on which they were run, CAM4, are described. These experiments were designed for the purpose of identifying the influence of specific AMV-related sea ice anomalies on the local atmosphere. The results of these experiments will be presented in Chapter 4. Finally, the second section of this chapter discusses some diagnostic methods that will be used throughout the thesis.

2.1 Climate model configurations

2.1.1 Atmosphere-ocean coupled model simulations

The CNRM-CM5 model

The CNRM-CM5 model was used for all atmosphere-ocean coupled model simulations in this thesis. CNRM-CM5 is a global atmosphere-ocean coupled climate model, usually used to simulate climate and to project future climate. The model has been described in detail by Voldoire et al (2013). It was developed as part of the Coupled Model Intercomparison Project 5 (CMIP5) suite of models (Taylor et al, 2012). The model uses the coupler OASIS3 to link together its three distinct components: the atmospheric component

ARPEGE-Climat together with the surface component SURFEX, the ocean component NEMO together with the sea ice component GELATO, and the runoff component TRIP.

The atmospheric component, ARPEGE-Climat, uses a semi-Lagrangian dynamical core. It has a 30 minute timestep, except for the radiative transfer module, which is instead called every three hours. It has a Gaussian grid with a horizontal resolution of 1.4° and 31 vertical levels. Obviously, with a single grid box spanning 1.4° by 1.4° degrees, many atmospheric processes cannot be resolved, and must instead be represented by parameterizations. Key parameterizations in the atmospheric component include those for longwave and shortwave radiation, aerosols, clouds, and large-scale precipitation, described in the references of Voldoire et al (2013). The ocean component, NEMO, uses a 1 hour timestep. It has a triangular grid with a horizontal resolution of 1° and 42 vertical levels.

In terms of model performance, CNRM-CM5 is overall similar to other CMIP5 in terms of its global seasonal cycle of historical climatology (Stocker and Coauthors, 2013). Furthermore, it has a realistic global energy budget and weak ocean temperature drift (Voldoire et al, 2013). Ruprich-Robert and Cassou (2015) evaluate the model in the North Atlantic, the region of interest here, and find that its mean ocean dynamics and deep convection zones correspond well with observations. However, despite overall broad agreement with observations, some major biases remain. Simulated precipitation compares poorly with observations in some regions, with excess precipitation in the tropical Southern Hemisphere being the prominent precipitation bias (Voldoire et al, 2013). Furthermore, large SST biases occur in the North Atlantic. Specifically, a cold SST bias of up to 6-7 °C occurs off Newfoundland, along with a negative salinity bias which compensates density. These biases are associated with a Gulf Stream and a North Atlantic Current that are inconsistent with observations (Ruprich-Robert and Cassou, 2015). Finally, the transport of cold, fresh water from the Labrador Sea to the midlatitudes is larger in CNRM-CM5 than observed (Ruprich-Robert and Cassou, 2015).

AMV initialization experiment design

To investigate the influence of the AMV phase on predictability and on the response to external forcing, four experiments were conducted using CNRM-CM5. These AMV initialization experiments were designed and performed by collaborators at CNRS-CERFACS (Centre national de la recherche scientifique - Centre européen de recherche et de formation avancée en calcul scientifique), and the output data was provided to us in the form of monthly data for each realization for a multitude of climate variables. Each experiment was initialized with a unique combination of AMV phase (+/-) and external forcing

(CO2/aerosols). In addition, unforced pre-industrial control (PICTL) integrations, with no imposed external forcing, were initialized from AMV +/- conditions.

Each simulation was initialized with extreme AMV conditions from either $AMV_{(+)}$ or $AMV_{(-)}$. For this, the same method was followed as described in Ménégoz et al (2018). One warm and one cold AMV period were selected from the CMIP5 CNRM-CM5 850-year pre-industrial control (PICTL) simulation. One year within each period was randomly chosen, and then used as the initial ocean conditions both for the PICTL and externally forced simulations during the corresponding AMV phase. Specifically, year 141 (303) was chosen to serve as initial conditions for the warm (cold) AMV case (stars in Fig. 2.1); these years represent extreme states of the opposite AMV phases. For each AMV state, 10 members of 30-year PICTL simulations were produced by varying only the atmospheric initial state.

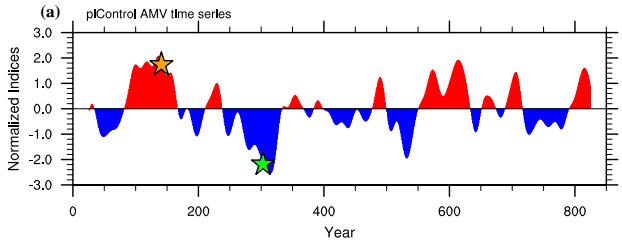

Figure 2.1: Annual normalized AMV index in the long CNRM-CM5 PICTL run. The years chosen for initialization of experiments are starred (orange star for $AMV_{(+)}$ initial conditions, green for $AMV_{(-)}$). From Ménégoz et al (2018). Reprinted by permission from Springer Nature Customer Service Centre GmbH: Springer Nature, Climate Dynamics, Role of the Atlantic Multidecadal Variability in modulating the climate response to a Pinatubo-like volcanic eruption, Ménégoz et al., Copyright 2018.

Two external forcings were separately applied: a 2% per year increase in CO_2 ("CO2"), and a linear aerosol increase ("AER"). For each initial AMV phase and each external forcing, an ensemble with 10 members of 30-year simulations was produced in the same manner as described above. The main focus is on the response to CO_2 forcing (Section 3.2.1); this will be compared to the response to aerosol forcing in Section 3.2.2.

Ensemble means, rather than the individual simulations, are shown, in order to isolate the forced response from short-term internal variability. Student's t-tests are used to determine whether significant differences exist between two ensemble means. The t statistic is calculated as

$$t = \frac{\overline{X}_1 - \overline{X}_2}{S_p \sqrt{\frac{1}{n_1} + \frac{1}{n_2}}}, \tag{2.1}$$

where

$$S_p = \sqrt{\frac{(n_1 - 1)S_1^2 + (n_2 - 1)S_2^2}{n_1 + n_2 - 2}}, \tag{2.2}$$

and where $\overline{X}_i$ is the ensemble mean of each experiment, S_i^2 is the ensemble variance, and n_i is the sample size. The associated P-value is the probability of the observed difference in means occurring, if the null hypothesis that the ensemble means were equal was true. If the P-value is less than 0.05, then the difference is said to be statistically significant at the 95% significance level.

Linear trends are used as a simple and intuitive representation of the net changes over the 30 year experiments. The validity of using trends was tested using epoch differential analysis, as in Deser and Phillips (2009). For various fields, the difference between the mean of the last 10 years and the mean of the first 10 years was calculated, and compared to the linear trend. The results from the two methods were nearly identical (not shown), showing that the linear trend is a good representation of the net changes.

The response to a given external forcing in a given AMV phase is calculated as the difference between the ensemble mean 30-year trends in the externally forced and the PICTL simulations initialized in that phase. For example, the response to CO_2 forcing in $AMV_{(+)}$ is given by the ($CO2_{AMV+}$ - $PICTL_{AMV+}$) ensemble mean trends. Throughout this thesis, for simplicity, the total response to each forcing is shown in the $AMV_{(+)}$ simulations only.

The component of the response to a given external forcing that is influenced by the AMV phase, termed the "AMV-related response", is calculated as the difference between the response, as defined above, in $AMV_{(+)}$, and that in $AMV_{(-)}$. For example, the AMV-related response to CO_2 forcing is given by [($CO2_{AMV+}$ - $PICTL_{AMV+}$) - ($CO2_{AMV-}$ - $PICTL_{AMV-}$)] ensemble mean trends. As all factors except the $AMV_{(+)}$ or $AMV_{(-)}$ initial conditions are held fixed, this gives the difference in the response that can be attributed to the initial AMV state.

2.1.2 Atmospheric model simulations

The NCAR CAM4 model

The NCAR CAM4 model was used for all atmosphere-only model simulations in this thesis. Unfortunately, although the atmospheric component of CNRM-CM5 can be run as

an AGCM, due to logistical issues this was not possible for this project. The NCAR CAM4 model is a global atmospheric climate model, usually used to simulate climate, often for the purpose of identifying the atmospheric response to certain sea ice concentration (SIC) or SST forcings. The NCAR CAM model has been described in detail by Neale et al (2013). The version used here is the CAM4 that is part of the Community Earth System Model (CESM) 1.0.4 (Kay et al, 2015). The model consists of active atmosphere and land components, while ocean and sea ice are prescribed.

CAM4 uses a finite volume Eulerian dynamical core. All simulations were run using 26 vertical levels and a finite volume grid with a horizontal resolution of 1.9x2.5°. This resolution was chosen as it was judged to be high enough for relatively good results, while also not being too computationally expensive. Higher horizontal resolutions were available and could have been used; however, while higher resolutions have been found to improve some aspects of CAM results, the improvements are not drastic (eg. Neale et al, 2013; Bacmeister et al, 2014) and were here judged not necessary given the associated higher computational expense. The simulations were run on the Compute Canada high performance cluster Graham using 2 nodes, with 32 tasks per node. With this set-up, the model ran at a rate of roughly 40 simulated years per day.

As CAM4 is an atmospheric model, any SST biases result from prescribed boundary conditions. Some deficiencies in the atmospheric model are that the CAM4 cloud fraction is too low with respect to observations, and therefore there are also biases in cloud radiative forcing in the model (Neale et al, 2013).

Sea ice forcing experiment design

Two pairs of simulations were designed, for the purpose of evaluating the atmospheric influence of AMV-related sea ice anomalies in the Greenland and Barents Seas. These simulations differed only by their prescribed sea ice concentration (SIC) and sea surface temperature (SST) boundary conditions, which are listed in Table 2.1 and described in more detail below.

Simulation Name	Description of Boundary Conditions
$CESM_{clim}$	CESM default PICTL climatology
$CNRM_{clim}$	CNRM PICTL climatology
$CESM_{perturbed}$	CESM climatology + regional $AMV_{(-)}$ SIC anomalies
$CNRM_{perturbed}$	CNRM climatology + regional $AMV_{(-)}$ SIC anomalies

Table 2.1: List and descriptions of AGCM experiments

Boundary conditions (prescribed SST and SIC) are a function of month, but not of year. Each simulation was run for 15 model years. To test for robustness, one simulation was run for 30 years, and compared to a 15 year run with the same boundary conditions. The response did not change significantly with the larger sample size, confirming that 15 years is long enough to obtain a robust response for these experiments. That a shorter run is sufficient for the atmospheric model simulations than used in the coupled model simulations is in part because of the types of experiments: in the atmospheric model runs, each year is the same, whereas in the coupled model runs have a time-dependent forcing and must therefore be run for longer.

The $\text{CESM}_{\text{clim}}$ boundary conditions are the default pre-industrial control boundary conditions for CAM4, which are derived from the average SSTs from 1870-1899 in the Merged Hadley-NOAA/OI (National Oceanic and Atmospheric Administration (NOAA) weekly optimum interpolation (OI)) Sea Surface Temperature & Sea-Ice Concentration dataset, described in Hurrell et al (2008). The $\text{CNRM}_{\text{clim}}$ boundary conditions are based on the monthly means from the long CNRM PICTL run, modified to the correct grid for use in CESM. The monthly means are linearly interpolated within the model to produce a time series of boundary conditions while maintaining the monthly mean. The anomalies prescribed on top of the CESM and CNRM climatologies in $\text{CESM}_{\text{perturbed}}$ and $\text{CNRM}_{\text{perturbed}}$, respectively, are identical in both cases. These anomalies are based on the monthly mean SIC anomalies (relative to the long CNRM PICTL run) in the $\text{PICTL}_{\text{AMV-}}$ ensemble, solely in the Greenland and Barents Sea region. Specifically, this is the region from 65°N-85 °N, 30°W - 60°E. Sea surface temperatures were not modified from climatological values, even where sea ice changes may have led to SST changes, in order to isolate the response due directly to SIC changes.

The reason for the focus on $\text{AMV}_{(-)}$, rather than $\text{AMV}_{(+)}$, is a logistical one. As shown below, the climatological sea ice is lower in $\text{CESM}_{\text{clim}}$ than in $\text{CNRM}_{\text{clim}}$. $\text{AMV}_{(+)}$ is warmer than climatology, so there are negative sea ice anomalies in the $\text{PICTL}_{\text{AMV+}}$ runs. These anomalies cannot be identically prescribed on top of the $\text{CESM}_{\text{clim}}$ and $\text{CNRM}_{\text{clim}}$ boundary conditions, as in some regions $\text{CESM}_{\text{clim}}$ does not have as much ice as was lost in the $\text{PICTL}_{\text{AMV+}}$ runs. Thus, in order to have identical anomalies in the boundary conditions in the perturbed runs, the positive SIC anomalies from $\text{AMV}_{(-)}$ are used.

The main focus in this thesis will be on the simulations with prescribed CNRM climatology. The simulations with prescribed CESM climatology will be briefly discussed in order to investigate the influence of a different background climatology on the response to sea ice forcing. The interest in this question is motivated later in the thesis (Section 4.3).

The annual mean of the anomalies in the boundary conditions are shown in Fig. 2.2.

Fig. 2.2a shows the SIC anomalies prescribed in the perturbed runs. SIC is higher in the region of interest relative to the climatological (control) runs; in $\text{AMV}_{(-)}$, as will be discussed later, there is anomalously high Arctic sea ice, particularly in this region. Fig. 2.3 shows the seasonal cycle of these sea ice anomalies.

Fig. 2.2b,c show the annual mean differences in climatological sea ice and SST, respectively, between the CNRM and CESM runs. In CNRM climatology, the northern hemisphere SSTs are largely colder while the southern hemisphere SSTs are warmer than those in CESM climatology. Consistent with the SST differences, in CNRM there is more sea ice in the northern hemisphere, and less in the southern hemisphere. As the CESM climatology is based on observations, these differences are consistent with the known biases with respect to observations in CNRM, some of which were discussed above.

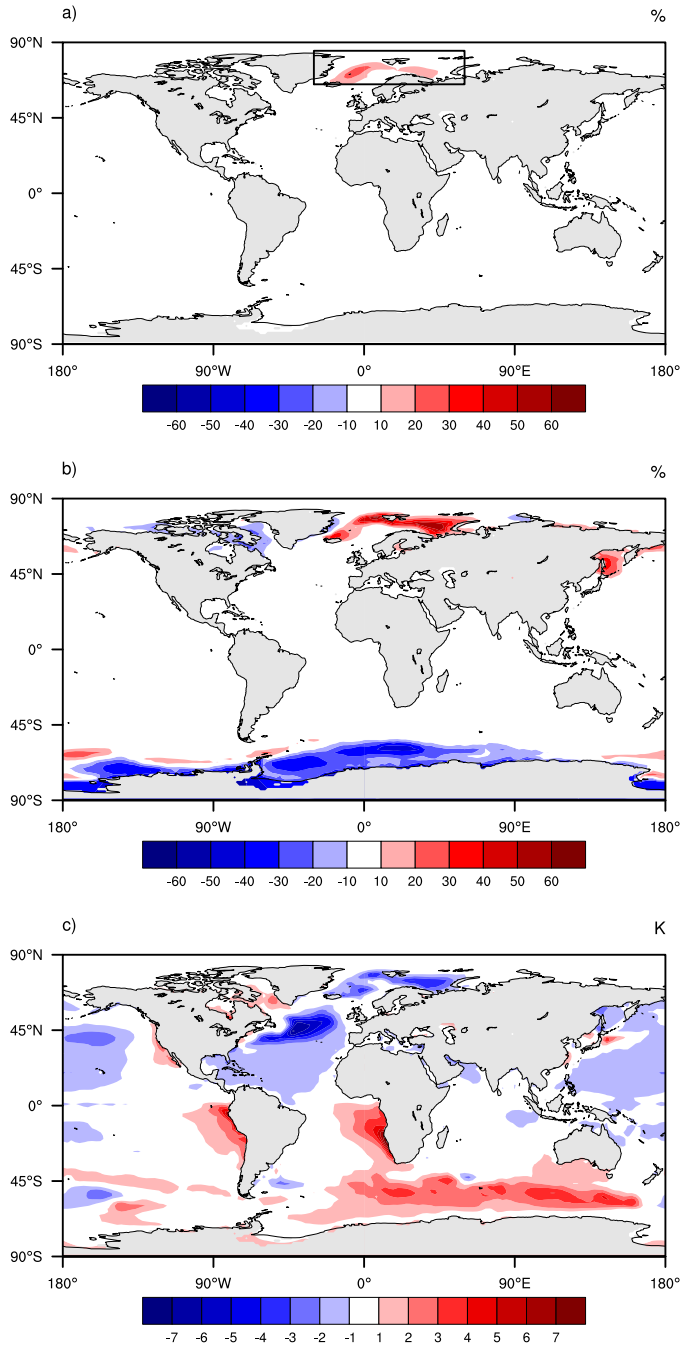

Figure 2.2: **a**) Annual mean of the AMV-related sea ice concentration anomalies (%) prescribed in the perturbed runs. The outlined region shows the area where $AMV_{(-)}$ sea ice anomalies were prescribed. The units are given in the top right hand corner. **b**) Annual mean of the difference in climatological sea ice concentration (%) in CNRM and CESM (CNRM-CESM). **c**) As in **b**, for SST (K).

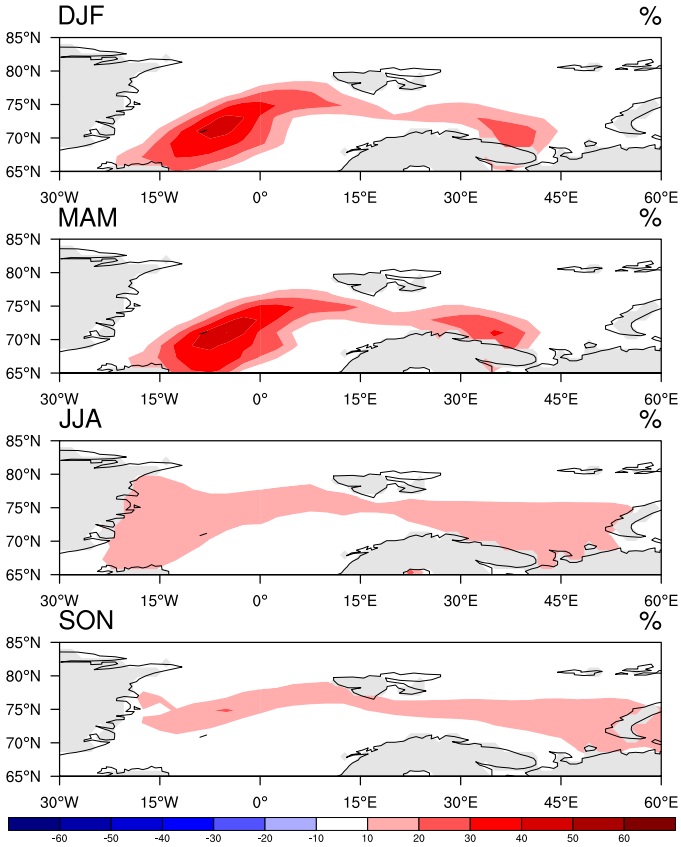

Figure 2.3: Seasonal means of the AMV-related SIC (%) anomalies prescribed in the perturbed runs. The region shown is the outlined region in Fig. 2.2**a**:, which is the only region where SIC anomalies are prescribed.

The AGCM response to $\text{AMV}_{(-)}$ Barents and Greenland Sea SIC changes is calculated as the difference between the perturbed and the climatological simulations with the same background climatology. The experiment design described here allows for the isolation of the atmospheric response to sea ice changes in this particular region. This can be compared to the coupled model results to elucidate the effect of the sea ice changes in the coupled model. However, note that even if the sea ice forcing were solely responsible for the atmospheric changes in the coupled model, the atmospheric anomalies in the coupled and atmospheric models would not be expected to be identical. First, model differences are expected to lead to some differences in the atmospheric response. Second, the lack of coupling in the atmospheric model means it cannot simulate any ocean-atmosphere feedbacks which occur in the coupled model. However, similar atmospheric anomalies in

the AGCM response to $AMV_{(-)}$ sea ice and the coupled model $AMV_{(-)}$ ensemble would suggest that sea ice has a dominant role in causing those anomalies.

2.2 Diagnostic methods

2.2.1 Constructed Circulation Analog Method

The constructed circulation analog method is a technique to determine the dynamical component of the anomalies in a variable. Here, it is used to separate the total anomalies in near-surface air temperature (TAS) into their dynamical and thermodynamic components. The dynamical component is defined as the anomaly originating solely through changes in atmospheric circulation, in the absence of changes in TAS due to direct radiative forcing. The thermodynamic component is the residual anomaly, and consists of anomalies due to direct radiative forcing as as well as changes in SSTs, land surface properties, and sea ice.

This method is described by Deser et al (2016b). For a given timestep (1 month) in a given ensemble member, a set of $N_a = 150$ of the closest sea level pressure (PSL) analogs from the CNRM 850-year PICTL run during the same month is found. "Analogs" with the target PSL field refers to states of the atmosphere which resemble that target. "Closest" is defined based on the Euclidean distance from the target PSL field in the domain of interest, which is the domain north of 20°N. The optimal linear combination of a random subsampling of $N_s = 100$ of the PSL analogs that best fits the target PSL field (that of the ensemble member) is then computed. This is done by expressing the target PSL field as a column vector X_h and the selected set of 100 analogs as a matrix X_s; then

$$X_h \sim X_s\beta = X_{CA}, \tag{2.3}$$

where β is a column vector of fitted regression coefficients, and X_{CA} is a constructed PSL analog. The value of β is determined from

$$\beta = X_s^{-1}X_h \tag{2.4}$$

by using a singular value decomposition to estimate the inverse of X_s. Finally, the associated dynamically induced component, Y_{dyn}, of a variable of interest, Y (here, TAS), is calculated as

$$Y_{dyn} = Y_s\beta, \tag{2.5}$$

where Y_s is the set of fields of Y from the same months as X_s. That is, Y_{dyn} is constructed using the same linear combinations of months from the CNRM long PICTL run as was used to construct X_{CA}. This process is repeated $N_r = 50$ times and the resulting average Y field is the dynamical component of the Y anomalies. The thermodynamic component, Y_{thermo}, is obtained as the residual

$$Y_{thermo} = Y_h - Y_{dyn}, \tag{2.6}$$

where Y_h is the Y field from the same month as X_h. The entire process is repeated for each time step of each ensemble member of each ensemble.

Deser et al (2016b) test the sensitivity of the result to the chosen values of N_s and N_r. They find that the results are robust to changes in both values, as long as the values are reasonably large ($N_s > 10$ and $N_r > 20$).

2.2.2 Climate Indices

The AMV index was calculated using the method proposed by Trenberth and Shea (2006): the annual mean AMV index was calculated as departures of North Atlantic SST (in the region 0 - 60°N) from the global mean SST (in the region 60°S - 60°N), and then smoothed using an 11-year running mean. In other work, the AMV index has been calculated as the linearly detrended, decadally filtered area-average North Atlantic SSTs (Enfield et al, 2001). This method was not appropriate here due to the linear detrending step, meant to remove the (assumed linear) secular anthropogenic changes in SST. However, since the simulations analyzed here do not contain a full AMV cycle, by linearly detrending, some AMV-related trends are removed. Therefore, the method proposed by Trenberth and Shea (2006) was more appropriate and was used instead.

As a measure of monthly mean atmospheric circulation in the northern extratropics and Arctic, the Arctic Oscillation (AO) index is used. The AO is the leading mode of internal variability in the Arctic (Thompson and Wallace, 1998). An AO index was calculated for each month of the CMIP5 850-year CNRM-CM5 PICTL simulation as the negative of the field mean north of 66°N of the monthly anomaly in 1000 hPa geopotential height (Z1000). This approximation is made because the positive AO is associated with a large negative pressure centered over the Arctic Ocean. The PSL and TAS patterns associated with the positive AO in the CNRM-CM5 model were then determined by regressing the 850-year PICTL simulation onto the calculated AO index. The area-weighted, uncentered pattern correlation with the AO pattern for the region north of 30°N was then used to quantify the resemblance of a given field to the positive AO.

Chapter 3

Results of AMV initialization experiments in a GCM

This chapter discusses the results of the AMV initialization experiments. The design of these experiments is presented in Section 2.1.1. The goal is to identify the influence of the AMV phase on the response to an external forcing, and investigate the mechanisms of this influence. First, the details of the AMV phase in the absence of any external forcing will be discussed. Second, the influence of the AMV phase on the response to CO_2 forcing will be investigated. Finally, the influence of the AMV phase on the response to aerosol forcing will be briefly investigated and compared to that with CO_2 forcing, in order to investigate which - if any - parts of the AMV influence on the response are robust to different external forcings.

3.1 AMV influence in the pre-industrial control climate

3.1.1 Mean AMV-related anomalies

In this section, the timescale of the predictability from the initial AMV-related ocean conditions is determined, to ensure that considering the 30-year simulations to be representative of a given AMV phase is justified. Then, the climatological anomalies associated with the AMV phase in the PICTL simulations are presented, and compared to the AMV in observations and other models. This is important as CNRM-CM5 must adequately model

the AMV; otherwise, the results found here would not be remotely applicable to nature. Further, identifying the background climate anomalies in $\text{AMV}_{(+)}$ and in $\text{AMV}_{(-)}$ is essential for understanding how this background influences the climate response to external forcing.

As discussed in Section 1.1.1, the initial ocean values of a climate model simulation have a measurable influence on the climate for only a limited time. While the extreme SST anomalies in the North Atlantic are associated with long predictability, this still raises the question of how the influence of the initial AMV-related SST values evolves over the 30-year long simulations. Fig. 3.1a shows time series of the AMV index over the 30-year PICTL simulations (excluding the first and last 5 years, due to the running mean). The ensemble spread, interestingly, is similar for all 20 years shown; note that while initially there would be zero spread, as the initial ocean conditions are the same within each ensemble, the averaging obscures this characteristic. The ensemble means of the $\text{AMV}_{(+)}$ and $\text{AMV}_{(-)}$ initialized simulations clearly remain distinct for all years shown, indicating predictability of at least that long. Not all ensemble members remain in the AMV phase they were initialized in; however, the ensemble mean remains in the initial AMV phase, although it may trend slightly towards a neutral AMV phase. This remains true for the experiments with external forcings applied (Fig. 3.1b,c). Thus, it makes sense to refer to the $\text{AMV}_{(+)}$ experiments as being in an $\text{AMV}_{(+)}$ phase throughout, and the same for $\text{AMV}_{(-)}$.

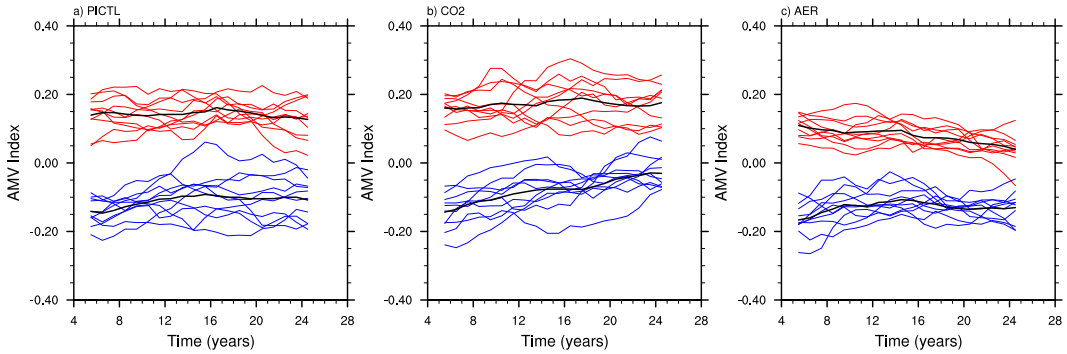

Figure 3.1: Smoothed AMV index for each realization with $\text{AMV}_{(+)}$ initial conditions (thin red lines) and $\text{AMV}_{(-)}$ initial conditions (thin blue lines), as well as their ensemble means (thick black lines), in **a**) PICTL, **b**) CO2, and **c**) AER.

The rest of this section will show the AMV climatology in the CNRM model and compare it with the literature. The northern extratropical pattern associated with the AMV phase is shown in Fig. 3.2 as the time mean difference between the $\text{PICTL}_{\text{AMV+}}$ ensemble mean and the $\text{PICTL}_{\text{AMV-}}$ ensemble mean. The near-surface air temperature (TAS) in

$AMV_{(+)}$ is the same or higher than that in $AMV_{(-)}$ nearly everywhere in the region of interest, consistent with Chylek et al (2009, 2010); Osborne et al (2017). Differences are particularly large in the Greenland and Barents Sea regions, associated with large differences in Arctic sea ice in these regions. This is consistent with observations (Miles et al, 2014). Snow cover and sea level pressure (PSL) anomalies are consistent with warmer temperatures in $AMV_{(+)}$, with mostly negative snow anomalies, and a low over the area of largest warm anomalies in $AMV_{(+)}$.

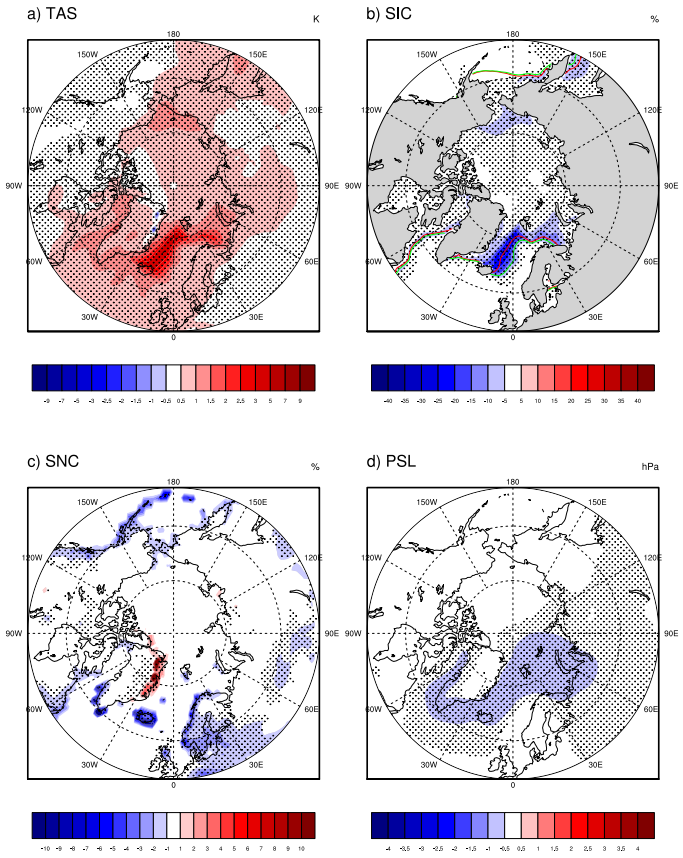

Figure 3.2: Difference ($AMV_{(+)}$ minus $AMV_{(-)}$) in climatological 30-year annual means in **a**) near-surface air temperature (TAS, K), **b**) sea ice concentration (SIC, %), **c**) snow cover (SNC, %), and **d**) sea level pressure (PSL, hPa). Areas where the difference is significant at a 95% significance level are stippled. In **b**, the contours show the mean climatological sea ice extent as defined by the 15% SIC line; the $AMV_{(+)}$ sea ice extent is shown in red and the $AMV_{(-)}$, in green. Units of % indicate the absolute percentage of the grid box that is covered by sea ice (as opposed to the relative percentage change in SIC). Where differences in means are too small to be seen but statistically significant, they are uniformly positive differences in TAS and negative in SIC.

The constructed analog method (Section 2.2.1) was used to determine the roles of dynamical and thermodynamic mechanisms in the mean AMV-related TAS changes. Fig. 3.3 shows the mean AMV TAS pattern ($AMV_{(+)}$ - $AMV_{(-)}$) in DJF and its breakdown into its dynamical and thermodynamic components. The focus is on DJF as this is when the AMV-related mean changes are largest, and (as justified later) as DJF will be the main season of interest in this thesis. From Fig. 3.3b, it is clear that the TAS anomalies are contributed to by AMV-related circulation changes, and (Fig. 3.3c) by thermodynamic mechanisms such as the direct influence of AMV-related SST and SIC changes. In general, both mechanisms lead to a warmer $AMV_{(+)}$/cooler $AMV_{(-)}$. There are some small (but significant) regions where dynamical changes induce cool anomalies in $AMV_{(+)}$, but these are countered by the thermodynamic warm anomalies. Both mechanisms contribute approximately equally to the maximum TAS anomaly over the Greenland and Barents Seas.

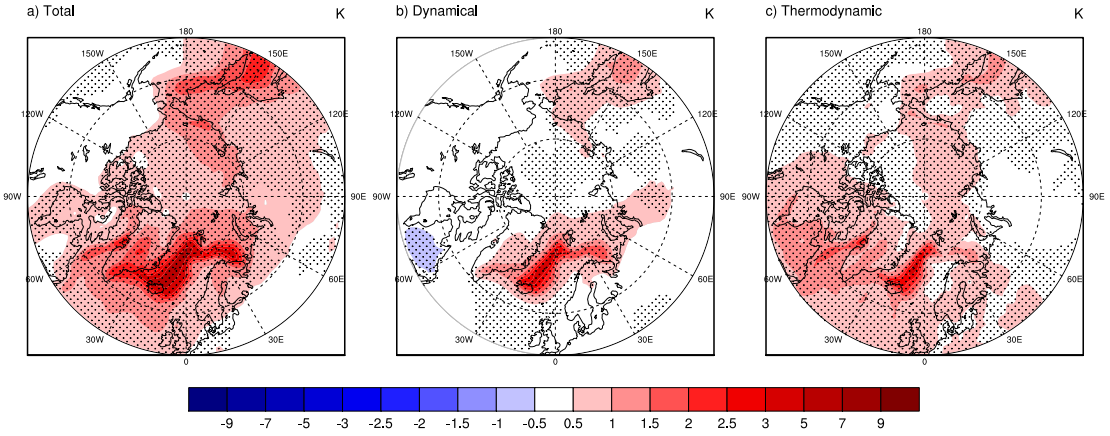

Figure 3.3: **a**) Total mean AMV pattern ($AMV_{(+)}$ - $AMV_{(-)}$), in PICTL DJF TAS (K), and its **b**) dynamical and **c**) thermodynamic components. Areas where the difference is significant at a 95% significance level are stippled.

Differences between AMV phases are not limited to the North Atlantic sector, despite the AMV being defined by the North Atlantic SST variations. There are also relatively large temperature and sea ice changes with AMV phase in the North Pacific sector (3.2). The AMV phase impacting the North Pacific SSTs is consistent with previous results (Lyu et al, 2017).

The AMV phase also influences climate in the tropical Pacific. Fig. 3.4 shows the DJF mean tropical precipitation anomalies associated with AMV phase. The AMV-related precipitation changes are largest in the tropical Pacific, with a drier western and wetter

eastern/central Pacific in the $AMV_{(+)}$ phase - i.e., a weakening of the Walker circulation. This is consistent with Vial et al (2018), who used a similar set of simulations.

The changes in the tropical and North Pacific may be related: Fig. 3.4 provides evidence for AMV-related changes in teleconnections between these regions. As discussed in Section 1.2, the Rossby wave source indicates where Rossby waves – which are the mechanisms for teleconnections – are generated; thus, the Rossby wave source changes shown in Fig. 3.4 suggest that differences in teleconnections exist between AMV phases. The anomalous largescale waves in eddy geopotential height at 250 hPa (Z250) reinforce this. Previous work (Lyu et al, 2017) has found that the AMV influences the Walker circulation and thus the teleconnections between the tropical and northern Pacific; however, they found a westward shift rather than a weakening of the Walker circulation in $AMV_{(+)}$.

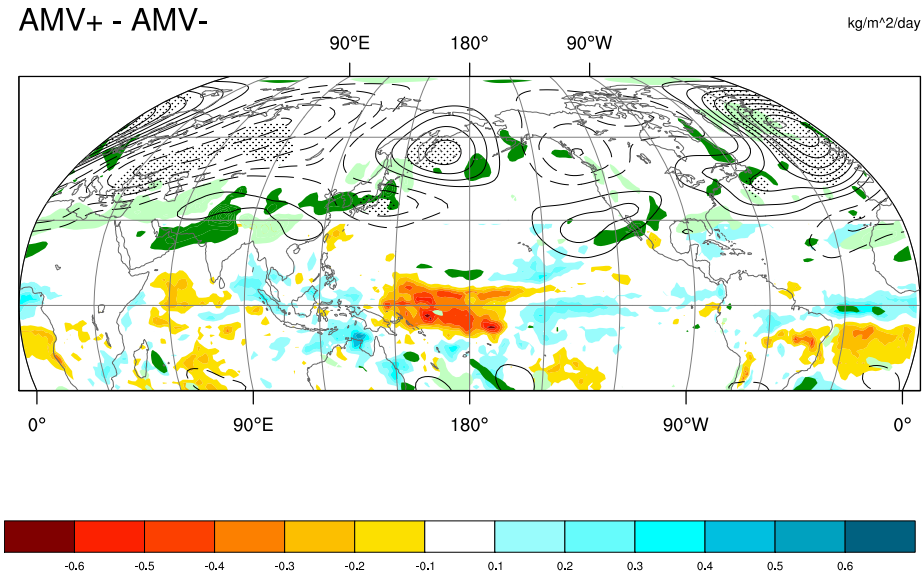

Figure 3.4: Mean AMV pattern ($AMV_{(+)}$ - $AMV_{(-)}$), in PICTL DJF precipitation (scaled shading), eddy Z250 (black contours), and Rossby wave source (green shading). Units of precipitation are $kg/m^2/day$. Precipitation differences above 30 N are masked, in order to only show tropical precipitation. Areas where the difference in eddy Z250 is significant at a 95% significance level are stippled. Negative contours are dashed. Each Z250 contour represents 2 m. Areas where the absolute value of the difference in Rossby wave source is larger than $1*10^{-11}$ s^{-2} are shaded in green; dark green indicates a positive value, while light green indicates a negative value.

In summary, the AMV-related anomalies in the CNRM-CM5 model are largely similar to those in observations and in other models. The AMV phase significantly influences

climatology not just locally, but in many regions, including the Arctic and the North and tropical Pacific.

3.1.2 Trends in the pre-industrial control

The time mean climatology associated with the AMV, as discussed in the previous section, is not the entire story for the PICTL simulations. The $AMV_{(+)}$ and $AMV_{(-)}$ simulations are started at an extreme point in the AMV cycle. Therefore, it is not surprising that over the 30 model years of the simulation - which is an appreciable fraction of the total AMV timescale of roughly 60-80 years - there are trends in the PICTL simulations, as the ensemble mean generally trends towards a neutral AMV phase. This effect is stronger in the $AMV_{(-)}$ runs, possibly because the randomly chosen $AMV_{(-)}$ initial ocean conditions are at a more extreme point than the $AMV_{(+)}$ initial ocean conditions (Fig. 2.1).

It is assumed that the directly AMV-related trends are the same in the PICTL and externally forced simulations. If this assumption were entirely true, then for each phase, by subtracting the trends in PICTL from those in the externally forced simulations, the trends that were directly related to the AMV initial conditions would cancel out, and what remained would be the trends due to external forcing - both those independent of and dependent on the AMV phase. However, identifying and describing the trends in the PICTL phase is still interesting.

Fig. 3.5a shows the annual temperature trends in $AMV_{(+)}$, and Fig. 3.5b shows the difference in these trends between AMV phases ($AMV_{(+)}$ - $AMV_{(-)}$). In $AMV_{(+)}$, there is a very small cooling trend in the region over Eurasia and the Barents and Greenland Seas, while in $AMV_{(-)}$ (not shown) there is a much stronger warming trend in this region. Therefore, the difference in trends is negative in this region. As the mean climatology is warmer in $AMV_{(+)}$ and cooler in $AMV_{(-)}$ (see Fig. 3.2), these trends are towards a neutral AMV in both phases (although much more strongly so in $AMV_{(-)}$).

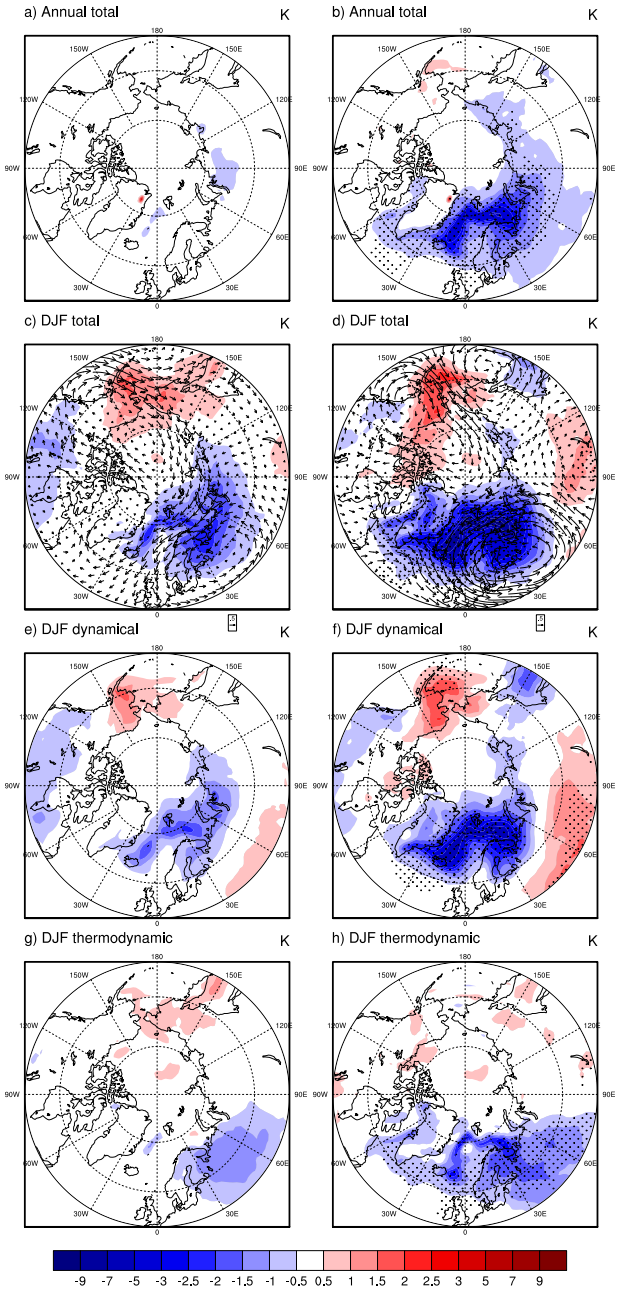

Figure 3.5: **a**) 30-year trend in PICTL total annual mean TAS (K) during the $AMV_{(+)}$ phase, and **b**) difference in said trend between AMV phases ($AMV_{(+)}$ minus $AMV_{(-)}$). **c,d**) As in **a,b** for total DJF mean TAS. Vectors show the same trends in the 850 hPa wind (units: m/s). **e,f**) As in **a,b** for dynamical DJF mean TAS. **g,h**) As in **a,b** for thermodynamic DJF mean TAS. Areas where the difference is significant at a 95% significance level are stippled.

The $AMV_{(+)}$ DJF TAS trends are shown in Fig. 3.5c, while the difference between phases is shown in Fig. 3.5d. The magnitude of the influence of the AMV phase on trends changes seasonally. The largest difference between AMV phases in the TAS trends is in winter (DJF), closely followed by spring (MAM, not shown). The differences in trends in MAM and DJF are quite similar. This remains true under external forcings, and therefore motivates the focus on DJF in this thesis. In DJF, as in the annual mean, there are more positive TAS trends in $AMV_{(-)}$ in the Greenland and Barents Seas. Also, there are more positive TAS trends in $AMV_{(+)}$ in central Eurasia and in the Bering Sea (although the difference in the latter region is not statistically significant).

The type of the mechanisms which force different TAS trends based on AMV phase can be identified by using the constructed analog method (see Section 2.2.1) to break the TAS trend differences down into their dynamical and thermodynamic components. In $AMV_{(+)}$ (Fig. 3.5e,g) dynamical processes are largely responsible for cooling over the Greenland and Barents Seas and over North America. Both dynamical and thermodynamic processes drive trends over the Bering Sea, where both have a warming influence, and over continental western Eurasia, where dynamical warming is countered by thermodynamic cooling. In the difference between phases (Fig. 3.5f,h), thermodynamic and dynamical processes are important in roughly the same regions as in $AMV_{(+)}$. The dynamical component dominates the total difference, while the thermodynamic component is smaller and largely restricted to regions near the North Atlantic. The trends in 850 hPa wind (Fig. 3.5d) show a more positive trend in southerly winds in $AMV_{(+)}$ over the Bering Sea, suggesting dynamical warming in this region occurs partly through advection.

There is evidence that the dynamical changes over the Bering Sea are associated with a Rossby wave teleconnection to the tropical Indian and Pacific Oceans. In $AMV_{(+)}$, there are drying trends in the western tropical Pacific, which are associated with trends in the Rossby wave source in the subtropical western Pacific and a hemispheric-scale Rossby wave that extends from the subtropics into the extratropics (Fig. 3.6a). (Refer to Section 1.2 for a description of these mechanisms.) In the difference in trends between AMV phases, differences in the equatorial precipitation trends (with more equatorial drying and increasing subtropical precipitation in $AMV_{(+)}$) are associated with different trends in the Rossby wave source and in Rossby waves themselves.

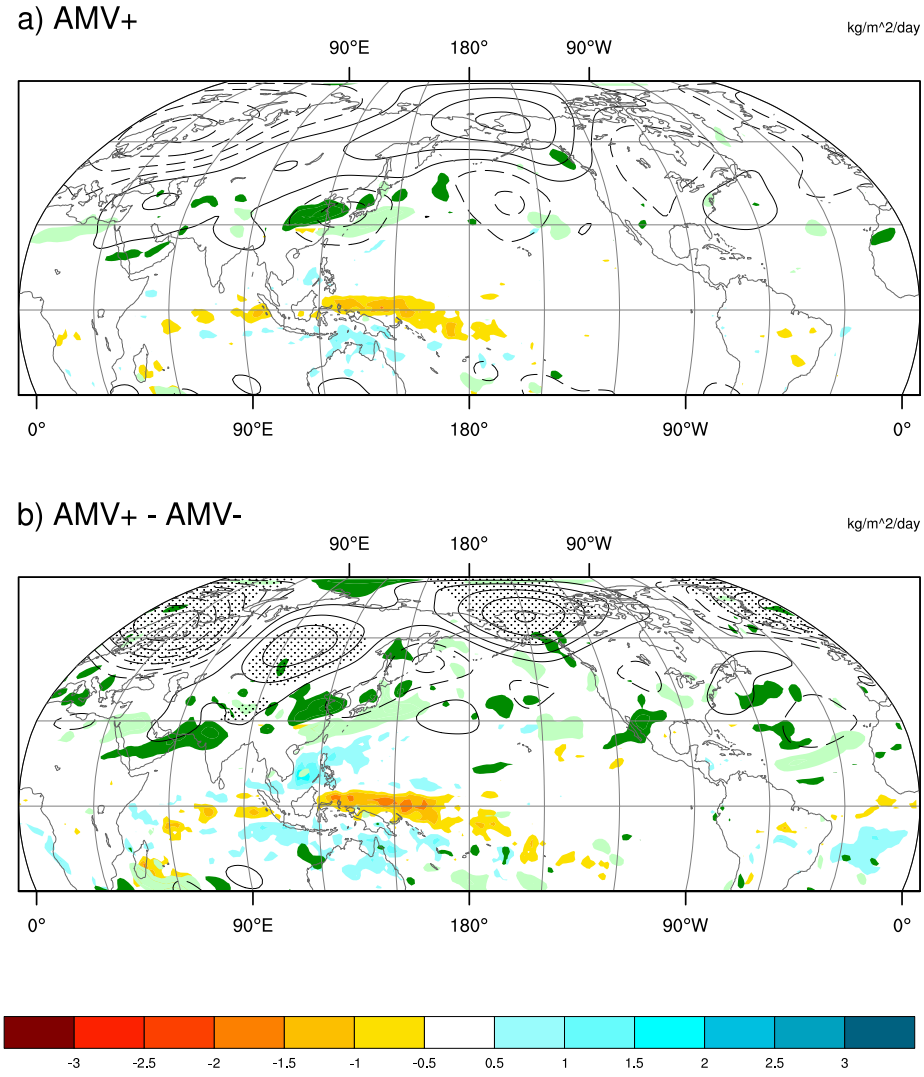

Figure 3.6: **a**) 30-year trend, during the $AMV_{(+)}$ phase, in PICTL DJF mean precipitation (scaled shading), eddy Z250 (black contours), and Rossby wave source (green shading). Units of precipitation are $kg/m^2/day$. Precipitation differences above 30 N are masked. Areas where the difference in eddy Z250 is significant at a 95% significance level are stippled. Negative contours are dashed. Each Z250 contour represents 10 m. Areas where the absolute value of the Rossby wave source is larger than $3*10^{-11}$ s^{-2} are shaded in green; dark green indicates a positive value, while light green indicates a negative value. **b**) As in **a**, for $AMV_{(+)}$ - $AMV_{(-)}$.

In summary, the AMV-related initial conditions influence climate for all 30 years of the simulations. In the PICTL simulations, the AMV phase changes the mean climate, with

$AMV_{(+)}$ warmer and less icy. Additionally, the specific initial (AMV-related) ocean initial conditions lead to climate trends. Mean anomalies and trends are both largest in DJF. Unsurprisingly, thermodynamic processes contribute more to trends in regions adjacent to the North Atlantic (where the AMV influence on the mean climate state is largest). In regions farther away, thermodynamic influences are small and dynamical influences clearly dominate, partially through teleconnections to the tropical Indo-Pacific. With this understanding of how the AMV phase and the specific initial conditions influence the PICTL climate, the AMV influence on the response to external forcing will now be investigated.

3.2 AMV influence on the response to external forcing

The global mean response to external forcing is shown in Fig. 3.7 for simulations with $AMV_{(+)}$ and $AMV_{(-)}$ initial conditions. The global mean temperature response to the applied CO2 forcing is an increase of approximately 2 K. An increase of 2 K over 30 years is a much faster warming than that projected for the real climate; this is because the applied forcing here (roughly a doubling of CO2 over 30 years) is a much stronger forcing than the range of likely emissions scenarios. The choice of a stronger forcing is not expected to negatively impact the relevance of the results, as changes in response to the forcing are mostly linear.

With each forcing, the response in $AMV_{(+)}$ and that in $AMV_{(-)}$ are very similar in temperature, sea ice, and precipitation. As the global mean response to external forcing largely does not change in different AMV phases, the focus for the remainder of this thesis will be on regional responses.

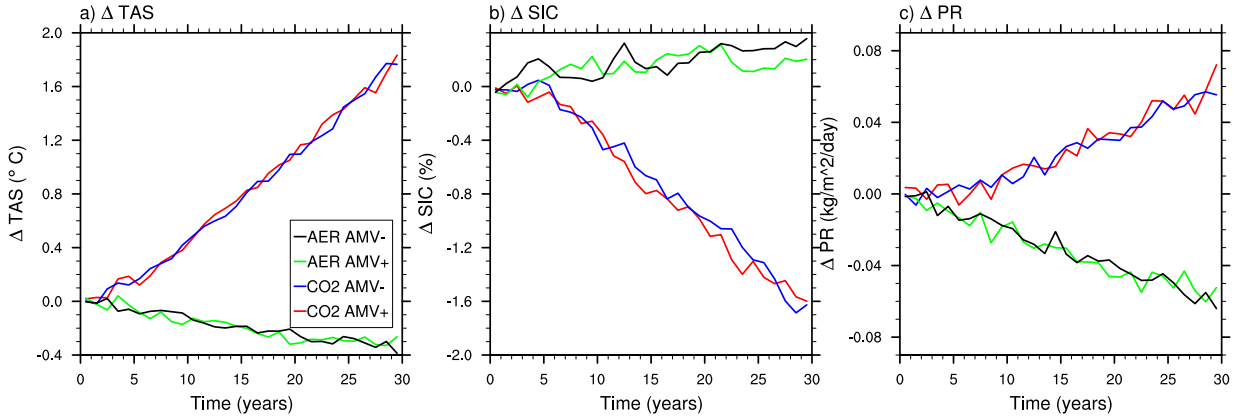

Figure 3.7: Time series of ensemble mean, global mean **a**) TAS (°C), **b**) SIC (%), and **c**) PR (kg/m^2/day) anomalies in response to each external forcing, in both AMV$_{(+)}$ and AMV$_{(-)}$.

3.2.1 CO2 forcing

The questions that will be explored in this section are (1) what is the AMV influence on the response to CO_2 forcing and (2) what physical mechanisms explain this influence?

The first of these questions is easy to answer. Fig. 3.8a shows the annual mean TAS response to CO_2 forcing (in AMV$_{(+)}$). As expected, warming occurs everywhere in the northern hemisphere extratropics, and is largest in the Arctic. Consistent with warming, snow cover and sea ice cover decrease (not shown), with the largest decreases in sea ice in the Greenland and Barents Seas. Fig. 3.8b shows the difference in this warming response between AMV phases. The AMV-related annual TAS response is a hemispheric-scale dipole: in AMV$_{(+)}$, continental Eurasia and the Barents and Kara Seas warm more, while North America, and parts of the extratropical North Pacific and North Atlantic warm less. Again, snow cover and sea ice have corresponding AMV-related responses, i.e. more (less) snow/ice loss in regions with more (less) warming.

Seasonally, the annual mean AMV-related response is dominated by the winter (Fig. 3.8d) and spring (not shown; similar to winter) responses. Therefore, compared to the annual mean, the DJF AMV-related response has a similar pattern but larger magnitudes. Specifically, there is more warming in AMV$_{(+)}$ in a region centered on the Barents Sea, and less warming in AMV$_{(+)}$ in North America and the North Pacific. The magnitude of the DJF AMV-related response is, in some regions, greater than 3 K; comparing Fig. 3.8c and Fig. 3.8d, this is clearly a significant fraction of the total response to CO2.

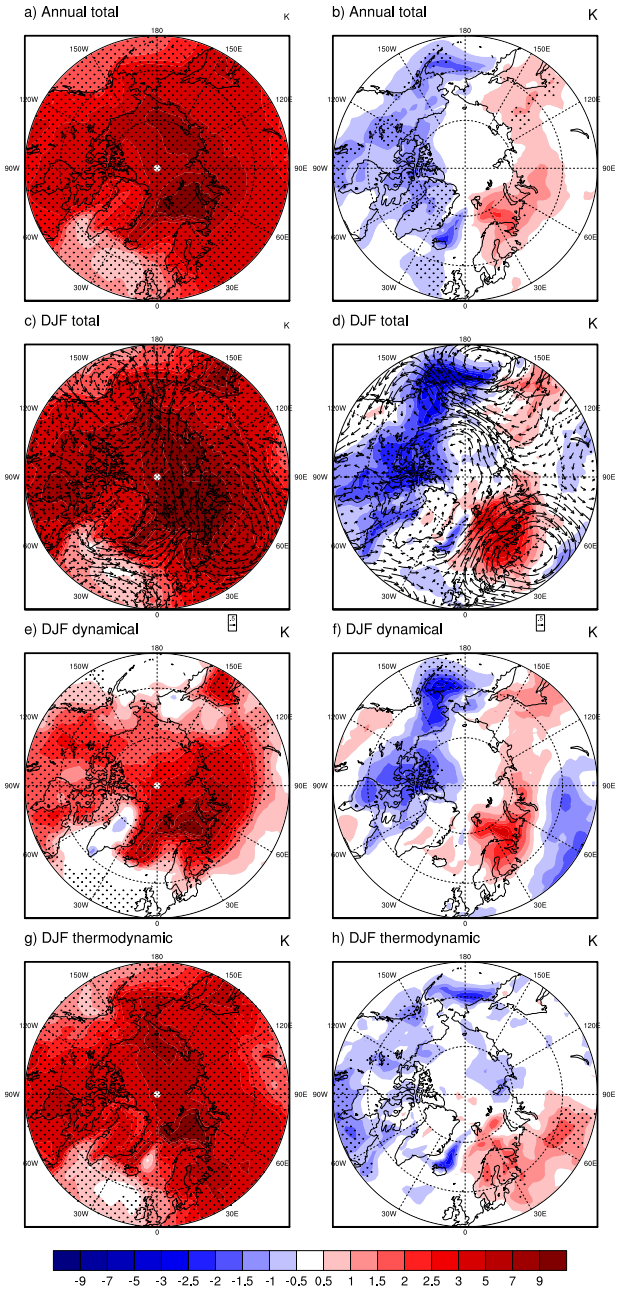

Figure 3.8: As in Fig. 3.5, for CO2-PICTL (i.e. response to CO_2 forcing).

In the remainder of this section, the physical mechanism which drive the spatial pattern

of AMV-related temperature response shown in Fig. 3.8d will be investigated. It is again useful to decompose the temperature response into its dynamical and thermodynamic components. The total warming in response to CO_2 (shown for $AMV_{(+)}$) has both dynamical (Fig. 3.8e) and thermodynamic (Fig. 3.8g) contributions. The thermodynamic component is dominant everywhere except over the Greenland and Barents-Kara Seas, where the dynamical component is of similar magnitude. Interestingly, for the AMV-related response, it is instead the dynamical component that dominates nearly everywhere (Fig. 3.8f): that is, while CO_2 forcing mainly acts through thermodynamics, the AMV mainly modulates the CO_2 forcing through atmospheric dynamics.

What specific processes drive the influence of the AMV on the dynamical response? First, the high-latitude AMV-related response has some similarities with the positive phase of the Arctic Oscillation (AO), a mode of internal climate variability in the high latitudes. The positive AO is characterized by a low in the central Arctic and highs in the North Pacific and Atlantic oceans, as well as a temperature dipole over the Arctic. Fig. 3.9a,b compares the pattern associated with the positive phase of the Arctic Oscillation in the CNRM-CM5 model (computed using the 850-year PICTL simulation) with the AMV-related response to CO2. In fact, the resemblance is not very good. The TAS patterns, despite both exhibiting a dipole, do not line up well, especially over North America and eastern Eurasia. The PSL patterns both exhibit a low over the central Arctic, but in the AMV-related response, the high-pressure center over the North Atlantic is shifted eastward by about 70°, and the high-pressure center over the North Pacific is shifted about 20° northward to be situated over the Bering Sea (Fig. 3.9b). Overall, the pattern correlation between the PICTL AO and the AMV-influenced response to CO_2 is only 0.29 (0.27) for TAS (PSL). This indicates that processes other than the AO likely explain the AMV-related dynamical response.

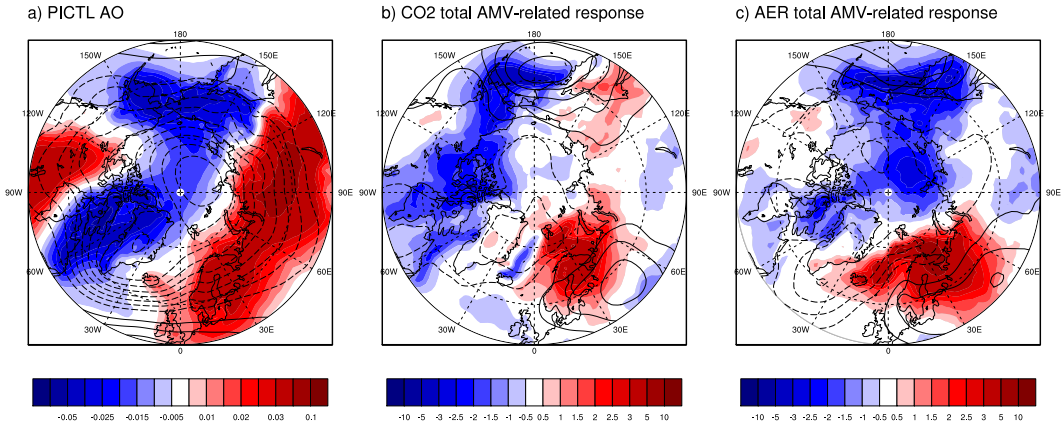

Figure 3.9: **a**) TAS (shading) and PSL (contours) of the 850-year PICTL simulation regressed onto the AO index. Shading shows the change in TAS per unit change in AO index (K/m). Contours show the same for PSL; each contour represents 2 Pa/m. **b**) TAS (shading) and PSL (contours) of the difference ($AMV_{(+)}$ - $AMV_{(-)}$) in the total DJF response to CO2. Shading shows the difference in trends in TAS (K) per 30 years. Contours show the same for PSL; each contour represents 1 hPa per 30 years. **c**) As in **b**, for AER.

Another possible mechanism for the AMV-related dynamical response is through teleconnections. In PICTL, and in previous work (Lyu et al, 2017), it has been found that the AMV phase influences teleconnections; thus, it is reasonable to speculate that AMV phase may influence the teleconnected response as well. Fig. 3.10 shows evidence that the AMV phase modulates the response to CO_2 in the North Pacific sector through its influence on a teleconnection with the tropical Pacific. In $AMV_{(+)}$, CO_2 forcing leads to increases in DJF equatorial precipitation and decreases in the northern subtropical precipitation. The Rossby wave source response to CO_2 is large in the subtropics, and it is associated with a zonal wave-2/3 Rossby wave response in the extratropics. The AMV-related precipitation response is in some regions larger than the precipitation response in $AMV_{(+)}$, as the AMV phase changes the sign of the precipitation response to CO_2. The largest AMV-related precipitation responses occur in the western tropical Pacific, with more drying in this region in $AMV_{(+)}$. Differences in the Rossby wave source response are large in the subtropics north of this region, and a large-scale Rossby wave train appears to radiate from the North Pacific, to North America, and into the Atlantic-European sector. This shows that a plausible mechanism for at least part of the dynamical AMV-related response in the Bering Sea is a teleconnection with the tropical Pacific.

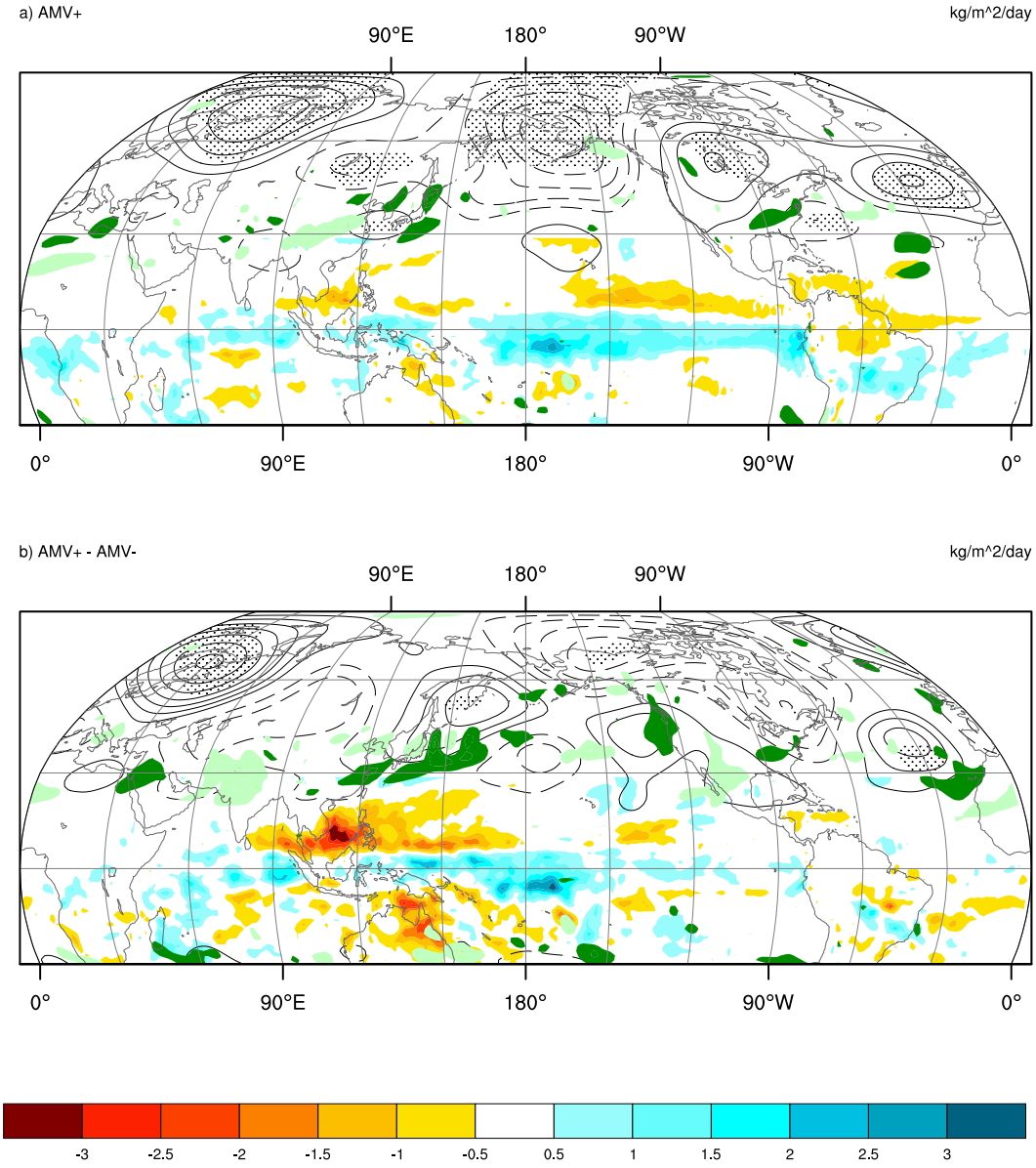

Figure 3.10: As in Fig. 3.6, for CO2-PICTL, with the exception that green-shaded areas are now where the absolute value of the Rossby wave source is larger than $5*10^{-11}$ s^{-2}.

The thermodynamic component of the AMV-related response to CO_2 is shown in Fig. 3.8h. Significant AMV-related responses occur mostly in the regions closest to the North Atlantic: in $AMV_{(+)}$, there is more warming over western/central Eurasia and the

Barents Sea, and less warming in eastern North America. The AMV-related response in the Barents Sea may be partially linked to sea ice processes: there is less (Fig. 3.2b) and thinner (not shown) initial sea ice in $AMV_{(+)}$ in this region. Under warming, SIC has been found to decrease more rapidly in areas of thin sea ice, both because the same decrease in SIC is created by a smaller volume of ice lost (Boé et al, 2010) and because the surface albedo feedback is more effective (Holland et al, 2006). The expectation is that in areas of lower sea ice, the positive surface albedo feedback is larger, increasing the amount of ice melted. Overall, more sea ice loss is expected in the Barents Sea in $AMV_{(+)}$, which could lead to more warming. However, while this could partially explain the AMV-related TAS response in the Barents Sea, the warming in western/central Eurasia spreads farther inland than expected if it were controlled by sea ice related mechanisms. One possible mechanism for the inland AMV-related TAS response would be differences between AMV phases in snow loss trends, and thus differences in magnitudes of local snow-related positive feedbacks. However, the AMV-related snow cover (SNC) response (Fig. 3.11) is largely insignificant or inconsistent with the AMV-related TAS response. An exception is central Eurasia, where the larger warming trend in $AMV_{(+)}$ is associated with a larger snow loss trend in that phase; however, it is not clear whether the higher temperature trends force the larger snow loss or vice versa. Overall, while more (less) warming in $AMV_{(+)}$ in western Eurasia (eastern North America) is largely attributable to thermodynamic processes, specific mechanisms are unclear.

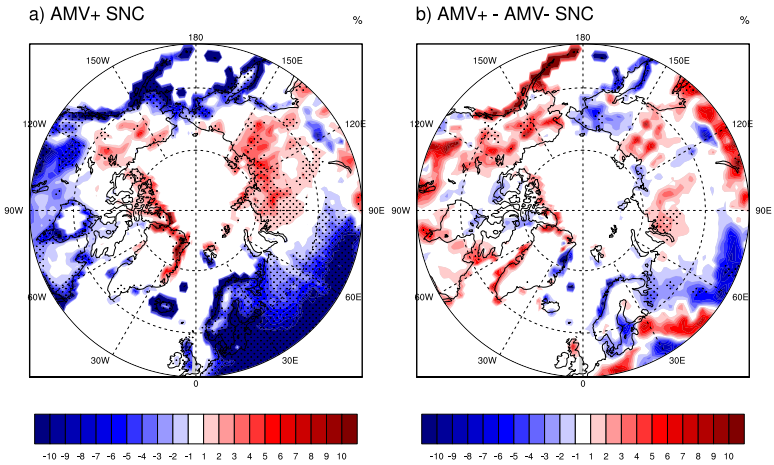

Figure 3.11: **a**) 30-year trend in CO2-PICTL DJF mean SNC (%) during the $AMV_{(+)}$ phase, and **b**) difference between phases in said trend ($AMV_{(+)}$ minus $AMV_{(-)}$). Areas where the difference is significant at a 95% significance level are stippled.

3.2.2 Comparison with aerosol forcing

The influence of the AMV on the response to a 2% per year increase in CO_2 was examined in the previous section. To what extent does the influence of the AMV on the response to an external forcing depend on the details of that forcing? This is investigated here by comparing simulations with an imposed anthropogenic aerosol forcing (AER) with the simulations of the previous section.

The aerosol forcing is different to the CO_2 forcing in several aspects. First, the magnitudes of these forcings are different, with the global mean temperature response to CO2 being about five times as large as that to AER (Fig. 3.7). Second, the geographic distribution of the forcings differ: the aerosol forcing is much more regional, and it is generally confined to the Northern Hemisphere over land and coastal areas. Finally, the sign of the forcing is different, with CO_2 having a warming effect and aerosols having a cooling effect, as discussed next.

The response to AER in $AMV_{(+)}$ is shown in the left column of Fig. 3.12, and the AMV-related response is shown in the right column. Fig. 3.12a shows cooling in response to aerosols, as expected: in the CNRM model, increased aerosol forcing leads to cooling across the northern extratropics through direct interaction with solar radiation and indirect interaction with clouds, which both act to increase planetary albedo (Voldoire et al, 2013). The aerosol cooling in these regions also drives increasing sea ice and snow cover (not shown). The annual AMV-related temperature response is small (Fig. 3.12b), largely because the influence of the AMV is very small in all seasons except winter. In DJF, there is a statistically significant AMV-related response, with less cooling in $AMV_{(+)}$ over western Eurasia and the Greenland and Barents Seas, and more cooling over the North Pacific and the central Arctic (Fig. 3.12d).

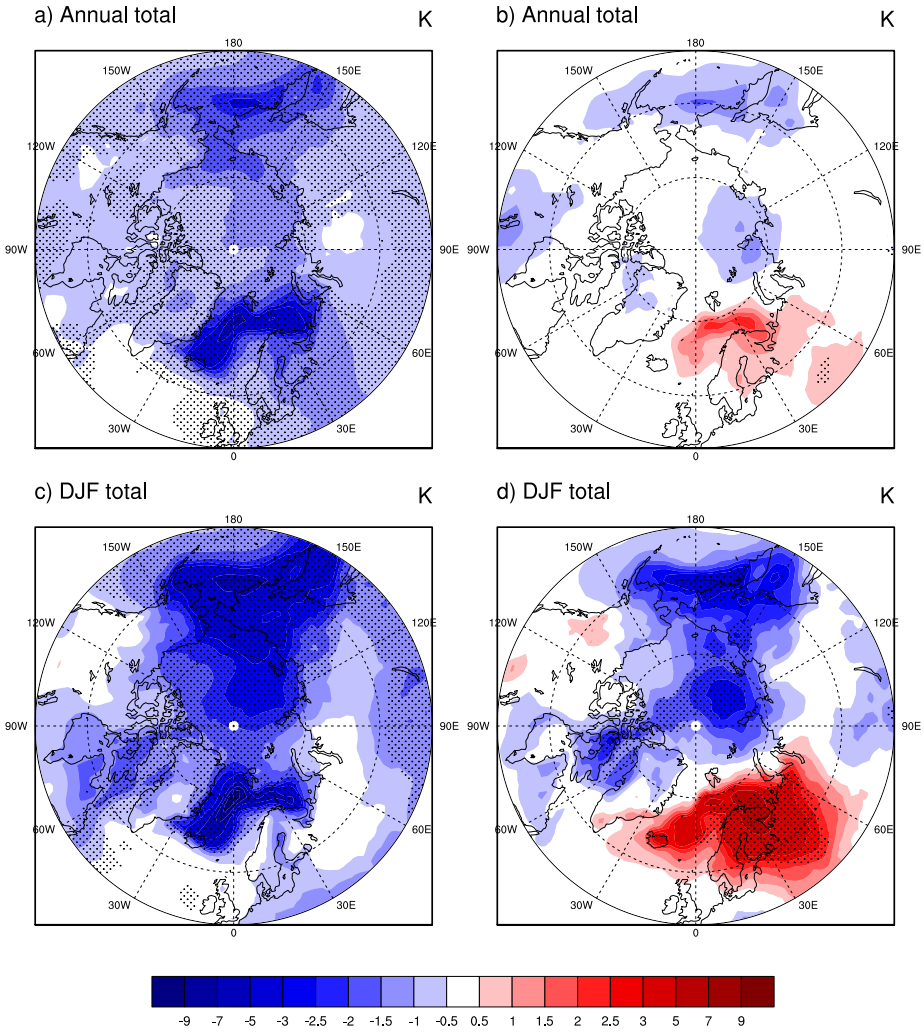

Figure 3.12: **a,c**) 30-year trend in AER minus PICTL annual and DJF mean TAS (K) during the $AMV_{(+)}$ phase, and **b,d**) AMV-related response in said trends ($AMV_{(+)}$ minus $AMV_{(-)}$). Areas where the difference is significant at a 95% significance level are stippled.

The $AMV_{(+)}$ response and the DJF AMV-related response to aerosol forcing have similarities to those to CO_2 forcing. In $AMV_{(+)}$, the response to aerosols is largest seasonally in DJF, and regionally in the Greenland, Barents, and Bering Seas. This is also the case under CO_2 forcing. The DJF AMV-related response to aerosols is a hemispheric dipole, although it is shifted westward relative to that under CO_2 forcing. As a quantitative comparison, the pattern correlation between the DJF AMV-related responses under CO_2 and aerosols, for the region north of 50°N, is 0.58; this indicates that the pattern of the AMV-

related response is partly independent of forcing in DJF. The spatial variance of the DJF AMV-related response under aerosol forcing is 154% of that in the CO_2 case; this indicates that the magnitude of the DJF AMV-related response is nonlinear with forcing and is in fact larger with the much smaller aerosol forcing (roughly -0.4 K global mean temperature change, compared to roughly 1.8 K for CO2).

Are aspects of the physical mechanisms driving the AMV-related response also robust to forcing? As under CO_2 forcing, the DJF AMV-related response (Fig. 3.9c) under aerosol forcing resembles the TAS pattern associated with the Arctic Oscillation. The pattern correlation of the DJF AMV-related response to aerosols with the AO pattern is larger than in response to CO_2: in PSL the pattern correlation is 0.65 and in TAS, 0.46. This suggests that the DJF AO response to AER is modified by AMV phase, specifically with a more positive AO response in $AMV_{(+)}$.

Also consistent with CO_2 forcing, there is a negative DJF AMV-related TAS response over the Bering Sea, the region previously found to be influenced by an AMV-related teleconnection under both PICTL and CO_2. Fig. 3.13 supports the idea that the response to aerosols in the North Pacific sector is influenced by a similar teleconnection. In $AMV_{(+)}$, aerosol forcing leads to increasing precipitation in the western tropical Pacific, and decreasing precipitation in the subtropical western Pacific as well as the tropical Indian Ocean. The Rossby wave source response is largest in the subtropics, and there is an associated Rossby wave response in the extratropics. In the AMV-related response, the largest and most widespread differences in the precipitation response are in the western tropical Pacific, where (comparing Fig. 3.13a and b) the $AMV_{(+)}$ and $AMV_{(-)}$ responses are opposite in sign, as well as in the Indian Ocean. As with CO_2 forcing, large differences between AMV phases in the Rossby wave source occur north of the large precipitation differences, and a large-scale Rossby wave train radiates from the North Pacific to North America. Therefore, the negative AMV-related TAS response in the Bering Sea under aerosol forcing appears to be —at least partially — dynamical, specifically explained by a teleconnection with the tropical Pacific. Further, the AMV-related responses to aerosols in Fig. 3.13b look remarkably similar to those to CO_2 in Fig. 3.10b. Quantitatively, the pattern correlation of the AMV-related tropical precipitation responses (between 30°S and 30°N) to CO_2 and to aerosols is 0.59, while that of the extratropical (north of 30°N) AMV-related eddy Z250 responses is 0.72. This similarity indicates that this component of the AMV influence on the climate response is robust independent of forcing.

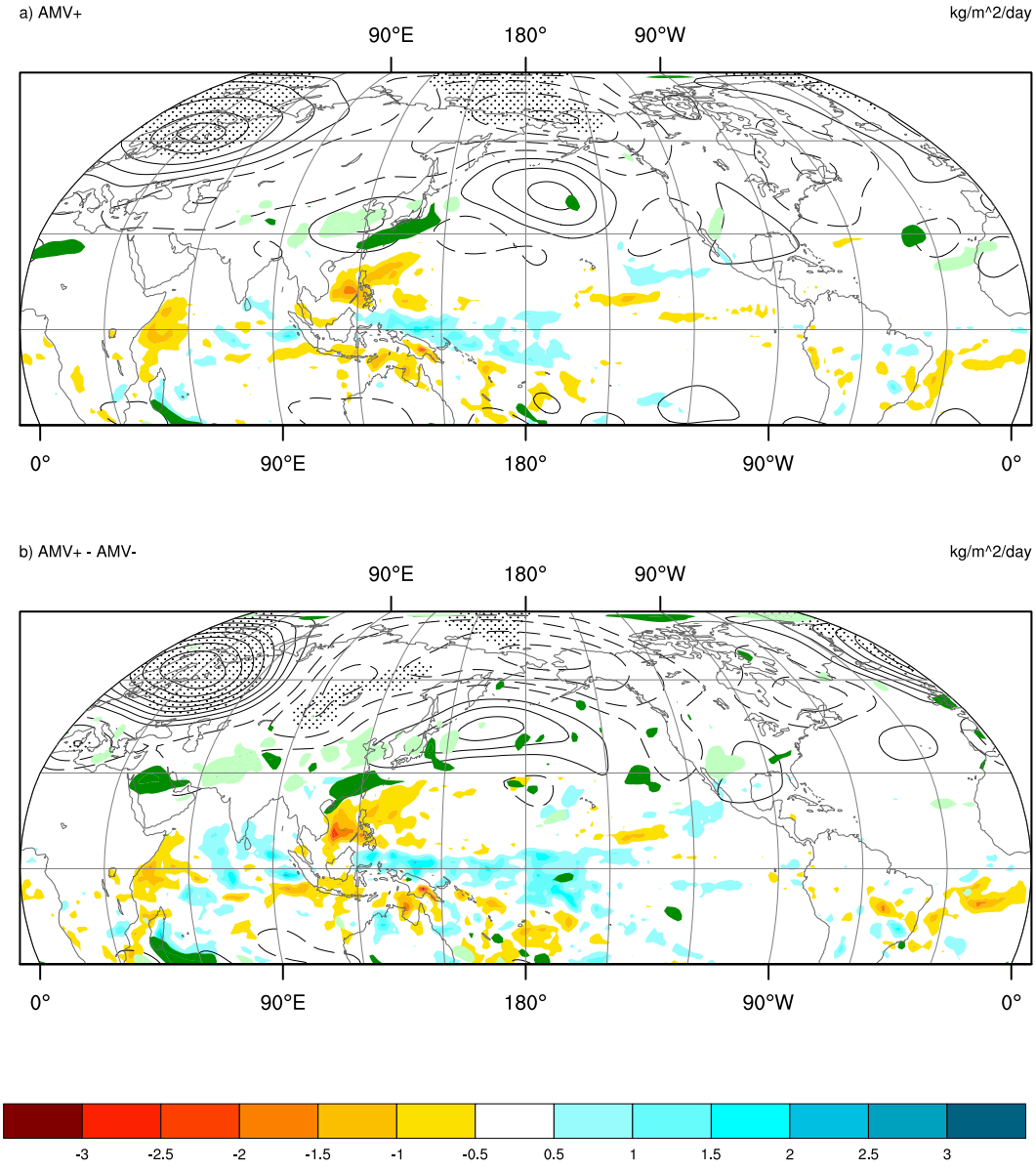

Figure 3.13: As in Fig. 3.10, for AER-PICTL.

Under aerosol forcing, the dipole in the AMV-related response is not evident in seasons other than DJF, not even MAM (during which it occurs under CO_2 forcing). Overall, while the annual mean AMV-related response is largely dependent on the applied forcing, many aspects of the DJF AMV-related response are similar under CO_2 and aerosol forcing.

Under both forcings, the AMV-related response exhibits a similarly oriented hemispheric-scale dipole. This may be partially due to a consistent influence of the AMV phase on the tropical Pacific response and the tropical teleconnections with the North Pacific.

Chapter 4

Role of sea ice in driving AMV-related atmospheric anomalies

In the previous section, externally forced coupled model experiments initialized in different AMV phases were analyzed, and some mechanisms through which the initial AMV phase influences the climate and the response to climate forcing were proposed. However, the interconnected nature of the coupled model leaves some uncertainties regarding cause and effect. For example, there are differences in air temperature and sea ice climatology and responses between AMV phases in the Greenland and Barents Seas, but is the sea ice forcing the atmosphere or vice versa? Using a climate model in atmospheric mode, in which SSTs and sea ice concentrations (SIC) are prescribed, is useful to investigate such questions, as it enables a more direct examination of cause and effect. A full description of the design of these atmospheric experiments, including the prescribed SST and SIC boundary conditions, can be found in Section 2.1.2

4.1 Understanding the coupled model ensemble mean response to AMV-related SIC anomalies

Here, the potential role of AMV-related sea ice anomalies in the Greenland and Barents Sea region in causing local atmospheric changes is investigated. From the AMV initialization experiments with the coupled model (Chapter 3), this is a region of interest: both dynamical and thermodynamic components contribute to AMV-related anomalies (Fig. 3.3)

in this region, the mechanisms for which are unclear. A pair of atmospheric general circulation model (AGCM) simulations with prescribed AMV-related sea ice anomalies in the Greenland and Barents Seas is used to investigate the impact of local sea ice and its role (if any) in forcing local atmospheric changes. As fully described in Section 2.1.2, the boundary conditions of $\text{CNRM}_{\text{perturbed}}$ are the $\text{AMV}_{(-)}$ sea ice anomalies in the Greenland and Barents Sea regions superimposed on CNRM 1850s climatology, while the boundary conditions of $\text{CNRM}_{\text{clim}}$ are the CNRM 1850s climatology. The atmospheric response to the SIC anomalies is the difference between the perturbed and control (climatological) runs. This design allows for investigation of whether local AMV-related sea ice anomalies the main mechanism for the pattern of AMV-related anomalies in TAS and PSL over the Greenland and Barents Seas.

If local sea ice anomalies are indeed the main drivers of the atmospheric response, then the expectation would be that, in the region of the prescribed sea ice anomalies, the time mean AGCM TAS response to the $\text{AMV}_{(-)}$ SIC anomalies would be very similar in both pattern and magnitude to the coupled model $\text{AMV}_{(-)}$ ensemble mean atmospheric anomalies. The heat flux response, PSL response, and the vertical structure of the atmospheric response would also be comparable to the anomalies in the coupled model in $\text{AMV}_{(-)}$. In response to sea ice forcing, the heat flux would be expected to show that the sea ice is forcing the atmosphere (negative heat flux anomalies) (eg. Screen, 2017). Seasonally, heat flux magnitude would maximize in DJF, when both the sea ice forcing is largest (Fig. 2.3 and the air-sea temperature difference is at its extreme, meaning the ocean rapidly loses heat to the atmosphere (eg. Deser et al, 2010). The expectation for PSL response is less certain, as previous studies have shown varying results, but most suggest that a high pressure anomaly would be associated with increased sea ice (Vihma, 2014). The expectation for the nature of the vertical structure (barotropic or baroclinic) is also somewhat uncertain. In a barotropic feature, density depends only on pressure, and large-scale motion does not depend on height, only on horizontal position and on time; this is contrasted with a baroclinic feature, where density depends on both pressure and temperature (Holton, 2004). The vertical structure of the response to sea ice changes may be expected to have both baroclinic and barotropic components, with the former a direct, localized response to the sea ice forcing, and the latter due to hemispheric-scale sea ice-induced changes in the large scale atmospheric circulation (eg. Deser et al, 2004; Alexander et al, 2004). In response to sea ice loss in (roughly) the Greenland Sea, Deser et al (2004) find that the total response is approximately equivalent barotropic.

Therefore, in this section, these aspects of the AGCM response are presented and compared to the coupled model AMV- atmospheric anomalies. Fig. 4.1 shows the annual and seasonal AGCM TAS response to the sea ice forcing, the coupled model TAS anomalies

in $AMV_{(-)}$ (from $PICTL_{AMV\text{-}}$), and the difference between them. The focus is on the same region in which the sea ice anomalies are prescribed.

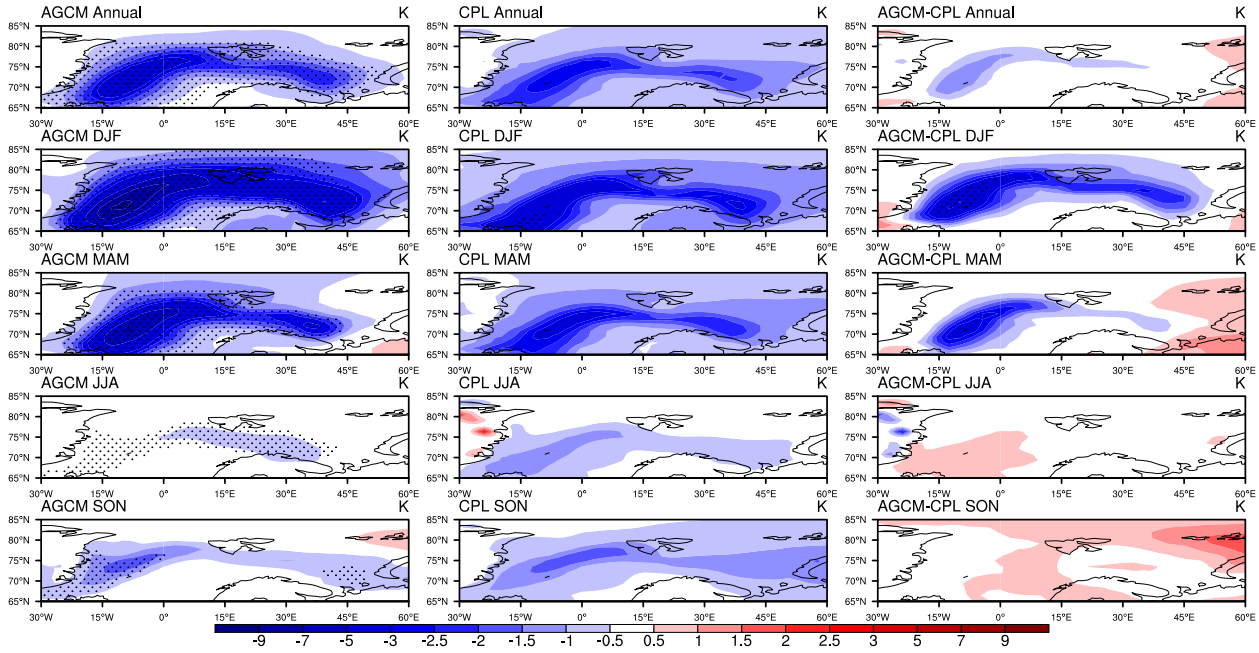

Figure 4.1: Left: AGCM TAS (K) response to local $AMV_{(-)}$ SIC anomalies, with CNRM background SST and SIC. Middle: Coupled model $AMV_{(-)}$ TAS (K) anomalies. Right: Difference between AGCM and coupled model $AMV_{(-)}$ TAS (K) anomalies. Note the non-linear scale. Areas where the difference is significant at a 95% significance level are stippled.

Qualitatively, the local TAS response to $AMV_{(-)}$ sea ice anomalies has a similar pattern to the coupled model TAS anomalies, with cool anomalies in the areas of sea ice gain. The seasonal cycle of temperature anomalies is also similar between both experiments, with the largest temperature anomalies in DJF and MAM. The magnitudes of the temperature anomalies are largely similar, with the exception of statistically significant larger anomalies in the DJF AGCM response in the Greenland Sea region.

Fig. 4.2 shows the same diagnostics for the turbulent surface heat flux. The pattern of $AMV_{(-)}$ heat flux anomalies in the coupled model is clearly very similar to that in response to the prescribed sea ice loss. Furthermore, the heat flux response is consistent with expectations if sea ice is forcing the atmosphere. The negative ocean-to-atmosphere heat flux in regions of sea ice change indicates that the sea ice increases are driving local atmospheric cooling. To the south and southeast of the region of sea ice gain, there are

positive heat fluxes. This is likely due to the cold air that is formed over the region of sea ice gain being advected south, and then warmed by the warmer, ice-free ocean there (similar to a mechanism reported by eg. Sun et al (2015) and Screen et al (2013) in the context of sea ice loss). The seasonal cycle is also consistent with expectations, with the largest heat flux responses in DJF.

While the pattern of heat flux anomalies is similar, the magnitudes of the DJF anomalous heat fluxes are larger in the coupled model than in the atmospheric model, by as much as 100 Wm^{-2}. Interestingly, this suggests that winter sea ice forcing to the atmosphere is larger in the coupled model, which seems incongruous with the smaller TAS change in the coupled model. This might be due to model differences between CAM and CNRM, or it could be an indication that a factor other than sea ice has an impact on the AMV-related TAS changes in this region in the coupled model, and partially counteracts the cooling due to sea ice gain.

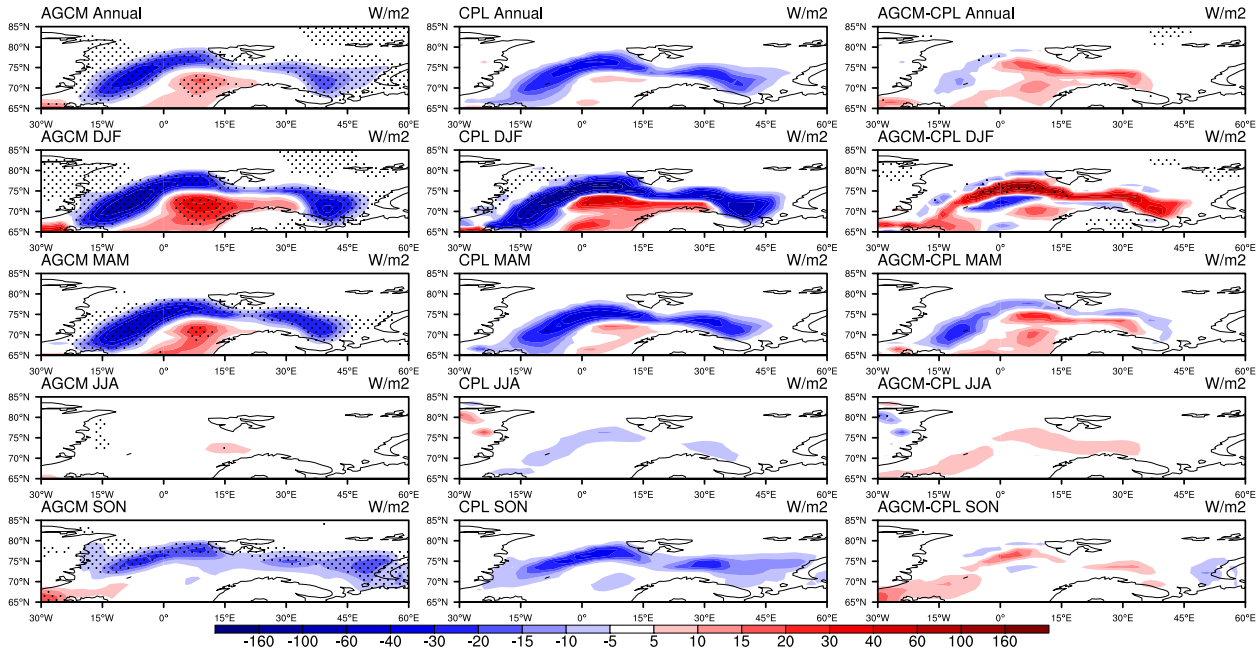

Figure 4.2: As in Fig. 4.1, for turbulent surface heat flux. Upward heat flux is defined as positive. Units are Wm^{-2}.

This analysis is repeated for PSL. Fig. 4.3 compares the PSL response to $\mathrm{AMV}_{(-)}$ SIC in the AGCM, and the PSL anomalies in $\mathrm{AMV}_{(-)}$ in the coupled model. There are some similar (although not statistically significant) PSL anomalies, specifically an anomalous

high in the Greenland Sea which occurs in most seasons and is largest in DJF. Anomalously high PSL can be associated with cooler surface temperatures; this, in combination with the similarity between the AGCM response and coupled model anomaly, suggests this anomalous high is locally forced by the $AMV_{(-)}$ sea ice changes. However, elsewhere the atmospheric model PSL response is quite dissimilar to the coupled model pattern, with anomalies of opposite signs over the eastern part of the region in DJF and MAM. This lack of similarity could be a result of model differences or lack of coupling, or could indicate that SST or SIC $AMV_{(-)}$ anomalies outside the region where anomalies were prescribed have a larger influence on the local PSL. It could also be contributed to by internal variability unrelated to the AMV; this possibility will be explored in the next section.

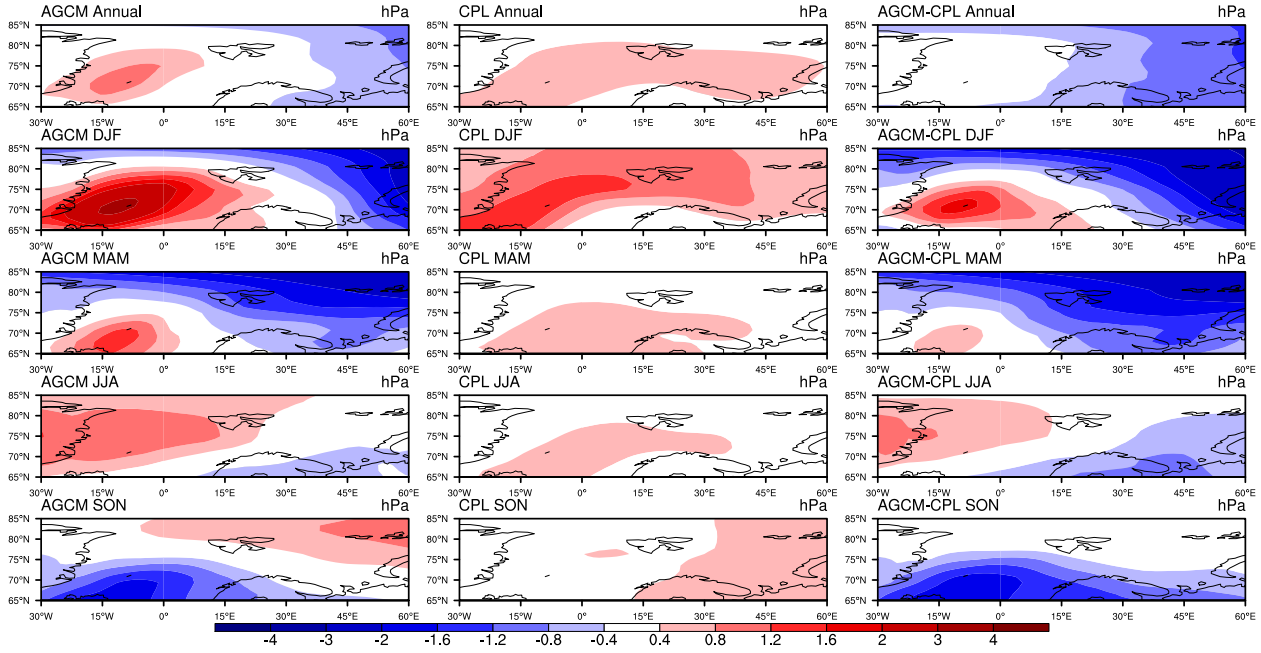

Figure 4.3: As in Fig. 4.1, for PSL. Units are hPa.

Finally, the vertical structure of the atmospheric response is investigated. A cross-section of the atmospheric anomalies at 75°N is shown in Fig. 4.4. (This latitude was chosen as the center of the region of interest; recall that the SIC anomalies are prescribed from 65°N to 85°N.) Fig. 4.4a shows the DJF eddy geopotential height (Z*) response to the $AMV_{(-)}$ SIC anomalies in the Greenland and Barents sea regions, while Fig. 4.4b shows the DJF mean Z* anomalies in $AMV_{(-)}$ in the coupled model. Vertically coherent features are barotropic, while vertically tilted features are baroclinic. In the coupled model, there

is a barotropic anomaly at approximately 0°E. The source of this anomaly is not clear. While the structure of the anomaly is somewhat consistent with that in Deser et al (2004), who find the total structure of the response to sea ice anomalies to be largely barotropic, the response can be contributed to by both baroclinic and barotropic components. Additionally, the structure of the AGCM response to sea ice loss is very different from the structure in the coupled model. This suggests that the vertical structure of AMV-related anomalies in the coupled model is not strongly driven by sea ice.

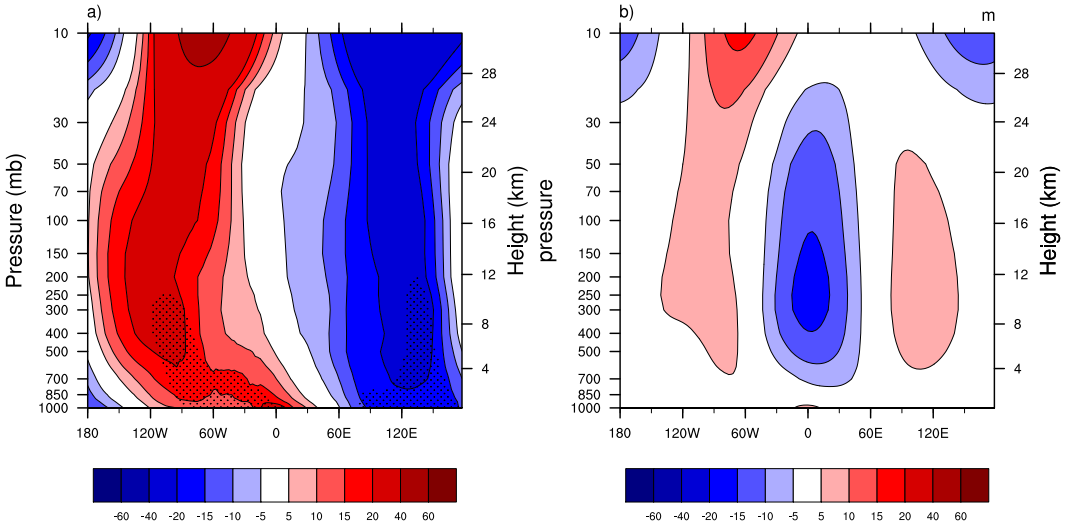

Figure 4.4: **a**) Z* DJF response at 75 °N to AMV$_{(-)}$ Greenland and Barents Sea SIC anomalies with CNRM background climatology. Recall that sea ice anomalies forcing were applied in the region between 30 °W and 60 °E. **b**) Z* DJF AMV$_{(-)}$ anomaly pattern at 75 °N in coupled model simulations. Areas where the response is significant at a 95% significance level are stippled. Units are m.

There is a large wave-1 response in the atmospheric model. This raises the question of whether the prescribed sea ice anomalies force any remote atmospheric changes. Fig. 4.5 shows the northern extratropical TAS response to the prescribed anomalies. There are cold anomalies to the immediate south of the forcing region in Scandinavia, and warm anomalies in central Eurasia, the Bering Sea, and the Beaufort Sea. These anomalies are, however, largely not statistically significant. They are also not consistent with the DJF temperature anomalies in AMV$_{(-)}$ in the coupled model, with the exception of the cool anomalies in Scandinavia. Overall, the temperature response to the Greenland and Barents Sea AMV$_{(-)}$ sea ice anomalies appears to be largely confined to the local region. Comparing with other work that has looked at remote temperature responses to sea ice changes in these regions, this is somewhat consistent with Screen (2017) in which it is found that, in general, large,

significant temperature responses to regional sea ice changes are restricted to that region. The small remote temperature changes forced by sea ice anomalies in the Greenland and Barents (and Kara) Seas found in Screen (2017) do not align with the responses found here, although that is not surprising given that here, the remote response is largely insignificant.

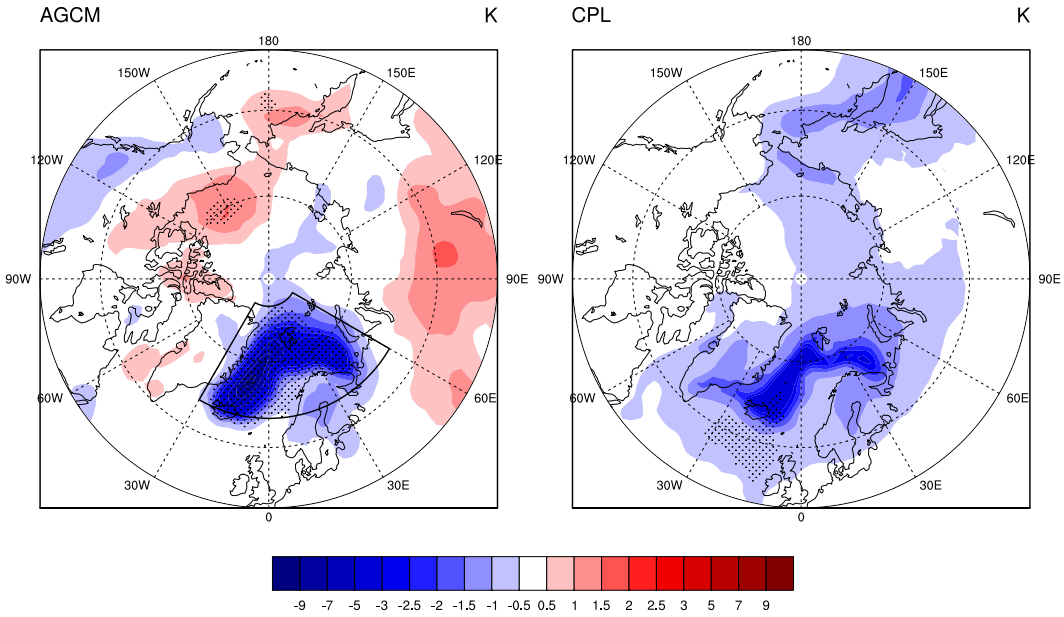

Figure 4.5: **a**) DJF TAS response (K) to $AMV_{(-)}$ Greenland and Barents Sea SIC anomalies. The outlined sector denotes the region where $AMV_{(-)}$ sea ice anomalies were prescribed. **b**) DJF TAS $AMV_{(-)}$ anomalies (K) in the coupled model. Areas where the response is significant at a 95% significance level are stippled.

4.2 Role of internal atmospheric variability

The coupled model anomalies discussed above are an ensemble mean of 10 30-year integrations, contrasted with the single 15-year integration in the atmospheric model. Averaging over the large ensemble in the coupled model essentially eliminates the internal climate variability that is not associated with the AMV. Thus, a natural question to ask is what role the internal climate variability has in the coupled response. Also, if internal variability plays a significant role, are there any individual realizations in the coupled model which have greater similarities with the atmospheric model response?

The degree of similarity between the annual TAS and PSL responses in the AGCM,

and the $AMV_{(-)}$ anomaly pattern in each individual coupled model realization, is shown in Fig. 4.6 using a Taylor diagram (Taylor, 2001). The reference field is the response to sea ice forcing in the region of $AMV_{(-)}$ sea ice anomalies only (i.e. outlined box in Fig. 2.2). The pattern correlation of each test field with the reference is represented by the azimuthal position of the point; the root mean square difference is represented by the distance from "REF"; and the ratio of standard deviation is represented by the radial distance from the origin.

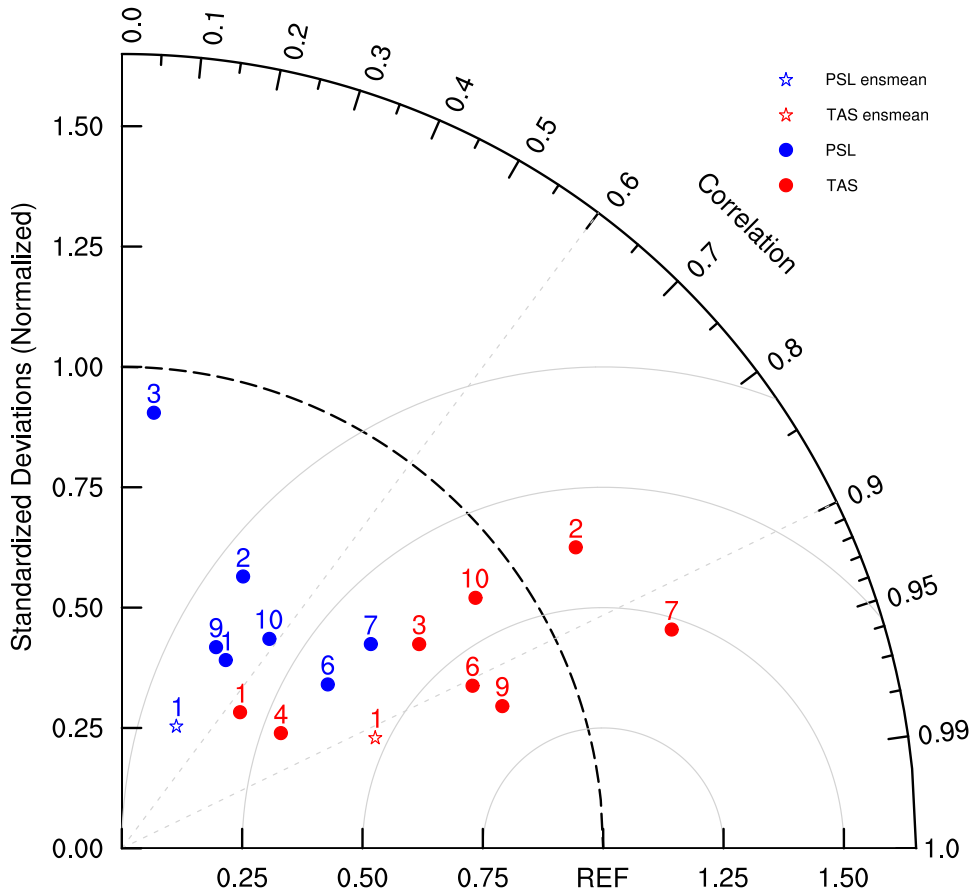

Figure 4.6: Taylor diagram comparing the local annual mean TAS (PSL) response to $AMV_{(-)}$ SIC anomalies in the AGCM with CNRM background climatology (reference) to the local annual mean TAS (PSL) $AMV_{(-)}$ pattern in each individual coupled model realization as well as the coupled model ensemble mean. Note that some realizations of the coupled model are not represented on the plot due to negative pattern correlations. For TAS, realizations 5 and 8 had, respectively, negative pattern correlations of -0.34 and -0.28, and variance ratios of 0.37 and 0.50. For PSL, realizations 4, 5, and 8 had, respectively, negative pattern correlations of -0.60, -0.71, and -0.77, and variance ratios of 0.19, 0.33, and 0.65.

For TAS, the pattern correlation of the coupled model realization anomalies with this field is generally quite high (with most values between 0.8 - 0.95, although note that two realizations are not represented on the plot due to negative pattern correlations). The ratio of variance is more variable, with some coupled model runs having much less variance and some slightly more. On average, the variance ratio appears lower than 1, consistent with the result from Fig. 4.1 that the anomalies are larger in the AGCM. The coupled model runs which compare best with the AGCM response tend to be those with anomalies close to the ensemble mean (not shown). As the AGCM is forced with the ensemble mean SIC anomalies from the coupled model, this would be an expected result if the local TAS anomalies are mainly forced by the local SIC changes. Overall, Fig. 4.1 and Fig. 4.6 show that AMV-related local TAS anomalies are similar in the two experiments.

There is a clear separation between the PSL and TAS fields, with the coupled model PSL anomalies being much less similar to the AGCM response. The ratio of the standard deviation is lower than 1 in all cases, indicating that the PSL anomalies are larger in the AGCM than the coupled model. From Fig. 4.3, this is not surprising. Additionally, the pattern correlation is generally lower than for the TAS response (note that three of the comparison points are not shown on the diagram due to negative pattern correlations). Compared to the ensemble mean (starred point), all individual realizations are more similar to the AGCM response in terms of the magnitude of their variance, and a few have higher pattern correlations. Internal variability, which may be largely averaged out in the ensemble mean, therefore has a significant role in the magnitude of the variance. In some cases, potentially where the contribution from internal variability is similar in the coupled and atmospheric model responses, it also increases the similarity of the pattern of those responses. However, even in these cases the similarity with the atmospheric model response is still quite poor.

Overall, the atmospheric model results show strong evidence that the AMV-related temperature changes in the Greenland and Barents seas are forced by local sea ice changes. The same cannot be said for the AMV-related PSL changes; however, the local PSL changes are almost entirely statistically insignificant in both the atmospheric and coupled model, and internal variability has a significant role in their magnitude. Thus, it seems that internal variability dominates any forced PSL response.

4.3 Quantifying the influence of the climatological SST and SIC

The AGCM simulations presented in Sections 4.1 and 4.2 were forced with climatological SST and SIC based on the CNRM model long PICTL run. As discussed above, this climatology is biased with respect to observations, and to the climatology of the atmospheric model used. Previous work has found that the atmospheric response to a sea ice forcing can be modified by the background SSTs (Balmaseda et al, 2010; Osborne et al, 2017) and SIC (Semenov and Latif, 2015). An obvious question is therefore whether the atmospheric response described above is robust to changing the background SST and SIC, such as to that consistent with observations.

This is investigated using a second pair of AGCM simulations, $\text{CESM}_{\text{perturbed}}$ and $\text{CESM}_{\text{clim}}$. $\text{CESM}_{\text{perturbed}}$ has the same prescribed SIC anomalies as $\text{CNRM}_{\text{perturbed}}$, but superimposed on a pre-industrial control climatology derived from available observations (Hurrell et al, 2008) rather than the CNRM PICTL climatology. Likewise, the prescribed SST and SIC in $\text{CESM}_{\text{clim}}$ are based on the observed climatology. Recall the differences in this climatology from Fig. 2.2: the observed climatology is warmer and less icy in the northern hemisphere, with the largest SIC differences in the Greenland and Barents Seas, and large SST differences in that region as well as in the North Atlantic. The differences in boundary conditions affect the simulated atmosphere; for example, there is lower Arctic cloud cover and precipitation with CNRM climatology (not shown).

Fig. 4.7 and Fig. 4.8 show, respectively, the TAS and PSL responses to the same anomalies as above, but with the background climatology derived from observations. Comparing these to Fig. 4.1 and Fig. 4.3 shows that, interestingly, the response to prescribed SIC anomalies in the AGCM depends not only on the anomalies themselves, but also on the background climatology. As with CNRM background climatology, the prescribed SIC anomalies lead to cooler local temperatures, and the seasonal cycle seen in the coupled model is roughly replicated. However, compared to the case with background CNRM climatology, the TAS patterns are not as similar to the coupled model anomalies. The PSL responses with CESM background are even more different: in all seasons but DJF they are of opposite sign to the coupled model PSL anomalies. The mechanism through which a warmer Northern Hemisphere background climate leads to these different responses is not obvious. Still, the strong influence of the Greenland and Barents Sea SIC anomalies on local TAS appears robust in DJF and MAM.

In summary, AMV-related sea ice in the Greenland and Barents Seas is found to have a key role in forcing local atmospheric temperature changes. This is robust to different

background climatologies. The local sea level pressure anomalies, however, are not dominantly driven by sea ice. These results enhance our understanding of the mechanisms of AMV-related changes in the coupled model. Specifically, in this region, local sea ice is a key mechanism for the AMV-related atmospheric temperature changes.

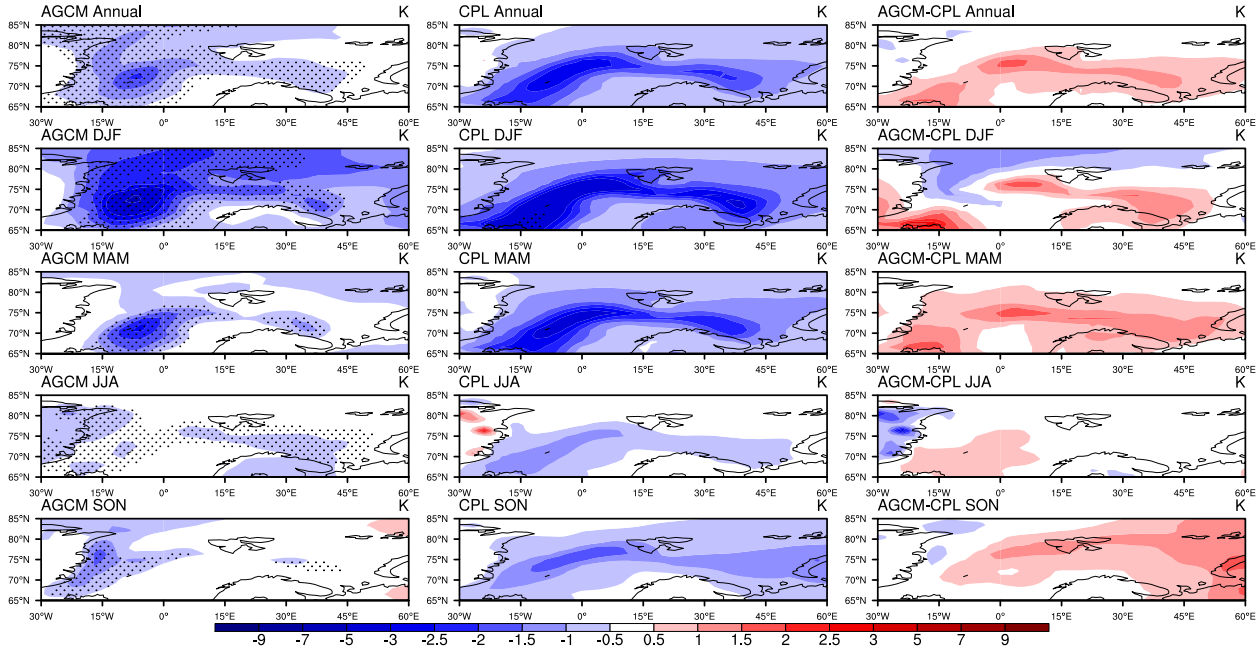

Figure 4.7: As in Fig. 4.1, for TAS and CESM background climatology. Units are K.

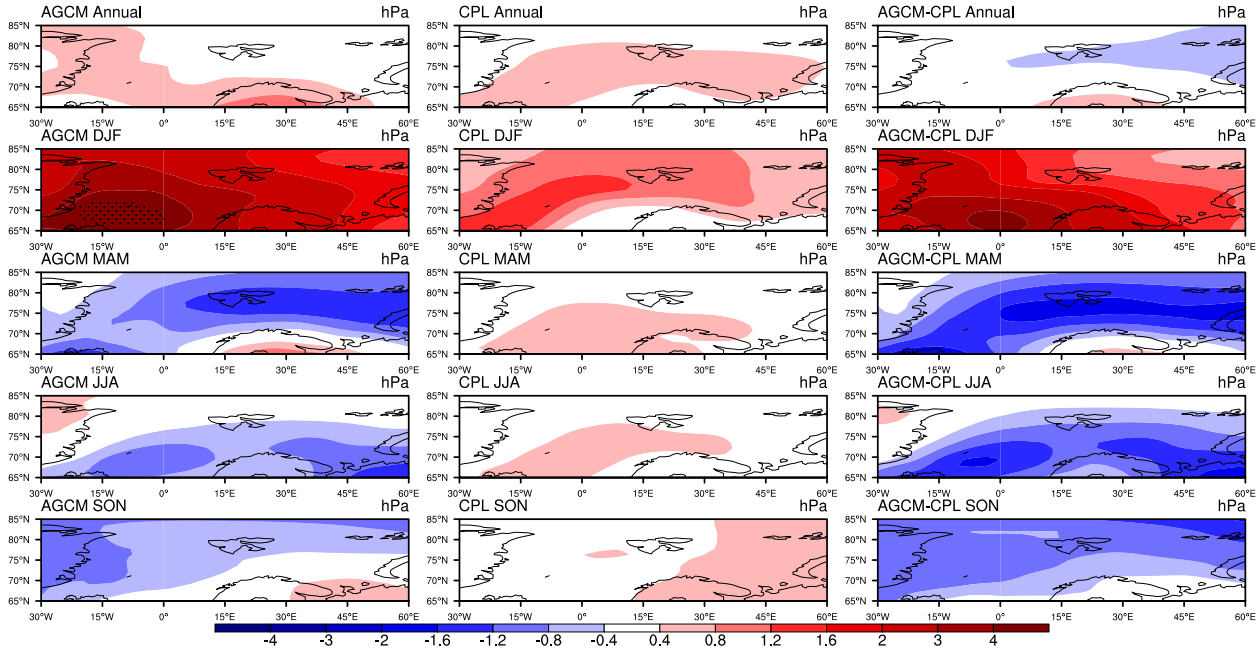

Figure 4.8: As in Fig. 4.1, for PSL and CESM background climatology. Units are hPa.

Chapter 5

Discussion and conclusions

5.1 Discussion

5.1.1 AMV initialization experiments (Chapter 3)

This section will summarize and discuss the results from the Atlantic Multidecadal Variability (AMV) initialization experiments, presented in Chapter 3. These experiments were used to investigate the influence of AMV phase on the response to external forcing (specifically CO_2 or aerosols). It was found that, although the AMV phase does not have a global mean impact on the response to external forcing, it has widespread influences on the regional response. Focusing on the northern extratropics, there is a hemispheric-scale dipole in the difference between AMV phases in the temperature response to CO_2. This "AMV-related response" is largest in winter (DJF), and is characterized by more warming in western Eurasia in the warm AMV phase ($AMV_{(+)}$), and more warming in North America and the North Pacific in the cold AMV phase ($AMV_{(-)}$).

The mechanisms of the winter AMV-related response were explored, partially through making use of a constructed circulation analog technique. The AMV phase largely modulates the dynamical, rather than thermodynamic, response to CO_2. Part of the dynamical mechanism driving the AMV-related response is an AMV-influenced teleconnection between the western tropical Pacific and the North Pacific. Previous work has found that the AMV phase impacts the tropical Pacific and its teleconnections with the northern Pacific (Lyu et al, 2017), and that the tropical Pacific response to forcing differs with AMV phase (Vial et al, 2018), so this mechanism is perhaps not surprising. Local thermodynamic

effects were found to have the most influence on the AMV-related response in regions adjacent to the North Atlantic. Again, this is perhaps not surprising, given that this is the region in which the AMV climatology is most different.

A potentially surprising result from these experiments was that the $AMV_{(+)}$ and $AMV_{(-)}$ ensemble means remained distinct from one another during the entirety of the 30-year simulations, and the $AMV_{(+)}$ and $AMV_{(-)}$ distributions clearly remained distinct from a climatological distribution. This suggests that, in the CNRM model, the North Atlantic has initial value predictability of at least three decades. This is somewhat inconsistent with previous findings, in which initial value predictability in the North Atlantic has been found to exist for up to a maximum of around 20 years (Msadek et al, 2010). However, extreme initial states have been found to have longer predictability (Griffies and Bryan, 1997; Collins et al, 2006), and the two ensembles here were initialized from extremes of the AMV phase. Additionally, the length of initial value predictability is highly model dependent. This combination of factors is likely largely responsible for the longer initial value predictability in the $AMV_{(+)}$ and $AMV_{(-)}$ ensemble here.

As mentioned in Section 1.3, previous work has examined the AMV influence on the response to external forcing. Specifically, both Osborne et al (2017) and Li et al (2018) have looked at how the AMV phase impacts the response to sea ice loss. As sea ice loss is associated with a warming climate, these results can be roughly compared to the response to CO_2 discussed above. The AMV-related atmospheric circulation response found here is largely dissimilar to that in Osborne et al (2017), where $AMV_{(+)}$ and $AMV_{(-)}$ SSTs are prescribed and the difference between AMV phases in the DJF atmospheric response to a warming forcing, in the form of sea ice loss, is examined. Somewhat surprisingly, in Osborne et al (2017) the AMV phase is not found to significantly modulate the response in the North Atlantic or Europe. In the Pacific-North American region, however, the response to sea ice loss does depend on the AMV phase. Osborne et al (2017) finds that various aspects of the response are different between AMV phases in this region: in $AMV_{(-)}$, (i) sea level pressure anomalies are more negative over the Aleutian islands and northeastern North America; (ii) there is less warming over the central-western Pacific and northeastern North America, and more warming over northwestern North America (linked with the sea level pressure AMV-related response); and (iii) in the 500 hPa geopotential height, there is an amplified trough-ridge-trough pattern in $AMV_{(-)}$, emanating from the central-western North Pacific. While a deeper (although westward-shifted) Aleutian low response in $AMV_{(-)}$ (Fig. 3.9) is also found here, this is the only region where the results here are similar to those in Osborne et al (2017). Elsewhere, it is found that the AMV phase modulates the North American response differently, and that here, unlike in Osborne et al (2017), the North Atlantic and European responses do indeed depend on the AMV phase,

with more warming in the European region in $AMV_{(+)}$, as well as a barotropic AMV-related circulation response in this region that may be connected to differences in the sea ice response. That different, as well as much more extensive, AMV-related responses were found here could be due to a number of reasons, including the type and size of the applied forcing, the lack of AMV-influenced SIC in Osborne et al (2017), or the lack of ocean-atmosphere coupling in Osborne et al (2017). In Li et al (2018), the Arctic Oscillation (AO) response to sea ice loss is found to depend on AMV phase: an AO- response occurs in $AMV_{(-)}$, but not in $AMV_{(+)}$. Therefore, their results are somewhat consistent with the more positive AO trend in $AMV_{(+)}$ under aerosol forcing found here, but not under the more similar CO_2 forcing.

Finally, in the AMV initialization experiments here, a weakness in the experimental design is that using only one coupled climate model means it is not possible to isolate which components of the response (if any) are model dependent. The results discussed in the previous paragraph, which were obtained using different models than here, suggest there may be some aspects of the response that are robust between models, but the extensive differences in experimental design limit comparison. Further experiments using similar forcing and other atmosphere-ocean coupled climate models would be required in order to investigate whether the results here are robust.

5.1.2 Sea ice forcing experiments (Chapter 4)

Sea ice forcing experiments in an atmospheric general circulation model (AGCM) were conducted to explore the role of sea ice anomalies in the Greenland and Barents Seas in forcing local AMV-related anomalies. The local near-surface air temperature (TAS) response to $AMV_{(-)}$ sea ice concentration (SIC) anomalies in the Greenland and Barents Seas was found to be very similar to the $AMV_{(-)}$ TAS anomalies in the coupled model. This supports the hypothesis that, in the coupled model, the AMV-related TAS anomalies in this region are indeed forced by the local SIC changes associated with AMV phase. In the context of the externally forced experiments here, this result suggests the hypothesis that the atmospheric AMV-related response to external forcing in the Greenland and Barents Sea region may, also, be driven in part by the sea ice changes. However, the sea level pressure (PSL) response was not as similar to the coupled model anomalies, suggesting that sea ice does not have as large a role in driving the PSL anomalies. Instead, AMV-related PSL anomalies in this region appear to be dominated by internal variability.

The TAS response to SIC was partially robust to background climatology: the response showed similar cool anomalies and seasonal cycle with both CNRM and observation-based

background climatology. Meanwhile, the PSL response to SIC was drastically changed by the different background climatology. That the background climatology had such an effect is not entirely surprising: He and Soden (2016b) force an AGCM with SSTs based on the climatologies of multiple different coupled models, and show that biases in the climatological SSTs can strongly impact climate change projections. Of the climate variables considered, sea level pressure was one of the most strongly impacted, while surface temperature was less impacted. Other work, such as Ashfaq et al (2011), has also found that SST biases lead to different projected changes in precipitation and temperature. Here, the similarities of the temperature response to changes in sea ice increases confidence in the relevance of the results to the natural world.

Limitations of the experiment design and of AGCMs may have affected the response to sea ice forcing found here. First, the prescribed sea ice anomalies are not precisely the same as the sea ice anomalies in the coupled model. The prescribed sea ice anomalies are the ensemble mean $AMV_{(-)}$ anomalies, repeated annually; the coupled model sea ice anomalies vary year-to-year as well as between realizations. The anomalies in each realization (not shown) are fairly similar to the ensemble mean, with almost all displaying a pattern of maximum sea ice anomalies in the Greenland and Barents Seas, although the magnitude of this pattern differs between realizations. (Compared to maximum ensemble mean annual mean SIC anomalies of around 20 % in the Greenland Sea (Fig. 2.2), individual ensemble members had maximum annual mean values of around 35 % on the high end, and less than 10 % on the low end.) The response to sea ice changes is not expected to be perfectly linear; therefore, absent any other errors or sources of forcing, the ensemble mean atmospheric anomalies in the coupled model would still not perfectly resemble the atmospheric response to the prescribed sea ice loss.

Second, the lack of ocean-atmosphere coupling in AGCMs is inconsistent with nature, as in reality the ocean and atmosphere do interact. The lack of ocean-atmosphere feedbacks in AGCMs, as mentioned above, has been found to damp the response to sea ice anomalies (Deser et al, 2016a; Smith et al, 2017). This does not appear to be the case here: instead, the temperature anomalies are larger in the atmospheric model with CNRM climatology than in the coupled model. However, there could be many reasons for the larger TAS anomalies in the AGCM, including model differences, differences in the SIC forcing (see previous paragraph) or in other sources of forcing not included in the AGCM experiments (such as AMV-related SST anomalies or SIC anomalies outside the region of interest), as well as lack of ocean-atmosphere coupling.

Finally, the prescribed SSTs were not modified in conjunction with the SIC anomalies. This was done to isolate the response solely due to sea ice forcing, but this method also has disadvantages. It excludes all SST changes, even those that may have been entirely due to

the sea ice changes. Also, it may create unrealistic temperature gradients at the surface (Screen et al, 2013), where ice has increased or formed, but SSTs have not cooled. Overall, despite these limitations of the model and the experiment design, given the robustness of the response and its strong similarities to the coupled model, it remains reasonable to conclude that local AMV-related sea ice anomalies are a main mechanism driving AMV-related TAS anomalies in this region.

5.2 Conclusions

In the coupled model AMV initialization experiments, the climatological AMV phases and their influence on the Arctic were found to be roughly consistent with expectations: in $AMV_{(+)}$, the Arctic was warmer and less icy, particularly in the Barents and Greenland Seas (Chylek et al, 2009, 2010; Miles et al, 2014). One surprising result was that, in all ensembles, the AMV initial conditions had a clear influence on the modelled climate for the length of the simulations (three decades). This is outside the range of North Atlantic initial value predictability found in the literature, which has only been found at up to two decades (Msadek et al, 2010). However, given the extreme initial values used here and the high model dependence of predictability, it is not entirely contradictory of previous results.

The AMV was found to influence the northern extratropical response to CO_2: the AMV-related response is a hemispheric dipole with more warming in $AMV_{(+)}$ in Eurasia, and more warming in $AMV_{(-)}$ in North America and the extratropical North Pacific. The differences in the response occur through both dynamical and thermodynamic mechanisms. In regions adjacent to the North Atlantic, where the AMV influence on climatology is largest, local thermodynamic AMV-related processes were most important. Elsewhere in the northern extratropics, dynamical influences (partially through tropical teleconnections) had a dominant role. Parts of the AMV-related response - including the teleconnected response - were found to be independent of the external forcing, with a very similar AMV-related response to CO_2 (climate warming) and aerosols (climate cooling) despite the different signs, magnitudes, and geographic patterns of these forcings.

The coupled climate model results are limited in that, due to the nature of the coupled model, cause and effect are very difficult to conclusively determine. Therefore, AGCM simulations with carefully chosen boundary conditions can be useful to isolate the influence of specific ocean or sea ice states. Here, AGCM experiments with $AMV_{(-)}$ sea ice anomalies prescribed in the Barents and Greenland Seas provided evidence that AMV-related TAS anomalies in this region are largely forced by local sea ice changes.

5.3 Future work

One logical next step is expanding this work to involve other climate models. Similar analysis could be performed using one or more different coupled GCMs to understand the role of model uncertainty in the results presented here. Confidence in the results found here would be greatly increased if they were found to be robust in other models. In related work, projects involving multi-model efforts to understand decadal climate variability are already exist and are underway. Specifically, Component C of the Decadal Climate Prediction Project (DCPP) invites climate modelling groups to produce experiments to study the origins, mechanisms, predictability, and regional imprints of particular long-term climate variations, including the AMV (Boer et al, 2016). This project makes use of restoration experiments, which use climate models which are fully coupled and evolve freely everywhere except in a regional of interest, where the ocean is restored to some desired sea surface temperature (SST). The DCPP includes experiments in which the North Atlantic SSTs are restored to $\text{AMV}_{(+)}$ or to $\text{AMV}_{(-)}$ values in a pre-industrial control climate, in order to investigate the climate response to this variability in multiple models in a systematic way (Boer et al, 2016; Ruprich-Robert et al, 2016). Another DCPP restoration experiment has inputs of historical external forcings and restored North Atlantic SSTs to observed anomalies over the period from 1950 to 2014, thus allowing for investigation of the role of variability in the North Atlantic in climate change during that time period. While neither of these experiments is directly comparable to the externally forced AMV initialization experiments discussed in this thesis, they show how multi-model projects can be, and are being, used to investigate climate variability.

This research has identified the influence of the AMV phase on the response to external forcing (albeit in only one model). This understanding of how the AMV phase modulates the response to external forcing could be applied to CMIP future climate projections, in order to evaluate whether the spread in climate change projections could be partially due to differing initial AMV phases.

Additionally, the methods used here could be applied to other modes of variability. On timescales of up to a few decades, internal variability is a dominant source of uncertainty in climate predictions (Hawkins and Sutton, 2009, 2011). (After this, uncertainties in the anthropogenic external forcing, as well as uncertainties between models, become more important.) Thus, on up to decadal timescales, it may be interesting to investigate the influence of other modes of variability in addition to the AMV on the response to external forcing. For example, similarly to the AMV, the Pacific Decadal Oscillation (PDO) is a long-term mode of variability that has been found in atmospheric models to influence the atmospheric response to sea ice (Screen and Francis, 2016), and is of interest in the

DCPP (Boer et al, 2016). The coupled model initialization method used here could be applicable to the PDO, and could be used to investigate whether it also influences the climate response to external forcing in a coupled model.

Finally, expanding on Chapter 4, much further work could be done using an atmospheric model (preferably, the atmospheric component of CNRM-CM5) to verify the specific mechanisms proposed here, as well as to investigate unidentified mechanisms. For example, such an experiment could be used to isolate the influence of AMV-related changes in the tropical Pacific on the response to external forcing, and therefore potentially confirm, as well as learn more about, the teleconnection mechanism discussed above. This could be done with a pair of simulations with boundary conditions that approximate CO_2 forcing (eg. a global SST increase) and AMV +/- SST anomalies in the Pacific (taken from the coupled model results). Similarly, the impact of AMV-related sea ice anomalies could be investigated in the presence of external forcing. By also decoupling the land surface model, the influence of AMV-related snow cover anomalies on the response to external forcing could be investigated. Restoration experiments, as discussed above, could also be used for similar purposes. This could be a better and more sophisticated modelling approach than atmospheric experiments, as restoration experiments avoid some of the issues inherent in atmospheric models, particularly the lack of coupling. These experiments could be used to gain further insight into the mechanisms through which the AMV phase influences the climate response to external forcing.

References

(2012) Teleconnection - AMS glossary. URL http://glossary.ametsoc.org/wiki/Teleconnection, Accessed: 2018-07-27

Alexander MA, Bhatt US, Walsh JE, Timlin MS, Miller JS, Scott JD (2004) The Atmospheric Response to Realistic Arctic Sea Ice Anomalies in an AGCM during Winter. J Climate 17(5):890–905, DOI 10.1175/1520-0442(2004)017⟨0890:TARTRA⟩2.0.CO;2, URL https://journals.ametsoc.org/doi/abs/10.1175/1520-0442%282004%29017%3C0890%3ATARTRA%3E2.0.CO%3B2

Alexander MA, Halimeda Kilbourne K, Nye JA (2014) Climate variability during warm and cold phases of the Atlantic Multidecadal Oscillation (AMO) 1871–2008. Journal of Marine Systems 133:14–26, DOI 10.1016/j.jmarsys.2013.07.017, URL http://www.sciencedirect.com/science/article/pii/S0924796313001693

Ashfaq M, Skinner CB, Diffenbaugh NS (2011) Influence of SST biases on future climate change projections. Clim Dyn 36(7-8):1303–1319, DOI 10.1007/s00382-010-0875-2, URL https://link.springer.com/article/10.1007/s00382-010-0875-2

Ba J, Keenlyside NS, Park W, Latif M, Hawkins E, Ding H (2013) A mechanism for Atlantic multidecadal variability in the Kiel Climate Model. Clim Dyn 41(7-8):2133–2144, DOI 10.1007/s00382-012-1633-4, URL https://link.springer.com/article/10.1007/s00382-012-1633-4

Bacmeister JT, Wehner MF, Neale RB, Gettelman A, Hannay C, Lauritzen PH, Caron JM, Truesdale JE (2014) Exploratory High-Resolution Climate Simulations using the Community Atmosphere Model (CAM). J Climate 27(9):3073–3099, DOI 10.1175/JCLI-D-13-00387.1, URL https://journals.ametsoc.org/doi/full/10.1175/JCLI-D-13-00387.1

Baines PG, Folland CK (2007) Evidence for a Rapid Global Climate Shift across the Late 1960s. J Climate 20(12):2721–2744, DOI 10.1175/JCLI4177.1, URL https://journals.ametsoc.org/doi/10.1175/JCLI4177.1

Balmaseda MA, Ferranti L, Molteni F, Palmer TN (2010) Impact of 2007 and 2008 Arctic ice anomalies on the atmospheric circulation: Implications for long-range predictions. QJR Meteorol Soc 136(652):1655–1664, DOI 10.1002/qj.661, URL http://onlinelibrary.wiley.com/doi/10.1002/qj.661/abstract

Bellomo K, Murphy LN, Cane MA, Clement AC, Polvani LM (2018) Historical forcings as main drivers of the Atlantic multidecadal variability in the CESM large ensemble. Clim Dyn 50(9-10):3687–3698, DOI 10.1007/s00382-017-3834-3, URL https://link.springer.com/article/10.1007/s00382-017-3834-3

Bjerknes J (1964) Atlantic Air-Sea Interaction. In: Landsberg HE, Van Mieghem J (eds) Advances in Geophysics, vol 10, Elsevier, pp 1–82, DOI 10.1016/S0065-2687(08)60005-9, URL http://www.sciencedirect.com/science/article/pii/S0065268708600059

Boé J, Hall A, Qu X (2010) Sources of spread in simulations of Arctic sea ice loss over the twenty-first century. Climatic Change 99(3-4):637–645, DOI 10.1007/s10584-010-9809-6, URL https://link.springer.com/article/10.1007/s10584-010-9809-6

Boer GJ, Smith DM, Cassou C, Doblas-Reyes F, Danabasoglu G, Kirtman B, Kushnir Y, Kimoto M, Meehl GA, Msadek R, Mueller WA, Taylor KE, Zwiers F, Rixen M, Ruprich-Robert Y, Eade R (2016) The Decadal Climate Prediction Project (DCPP) contribution to CMIP6. Geosci Model Dev 9(10):3751–3777, DOI 10.5194/gmd-9-3751-2016, URL https://www.geosci-model-dev.net/9/3751/2016/

Branstator G, Teng H (2010) Two Limits of Initial-Value Decadal Predictability in a CGCM. J Climate 23(23):6292–6311, DOI 10.1175/2010JCLI3678.1, URL https://journals.ametsoc.org/doi/10.1175/2010JCLI3678.1

Branstator G, Teng H, Meehl GA, Kimoto M, Knight JR, Latif M, Rosati A (2012) Systematic Estimates of Initial-Value Decadal Predictability for Six AOGCMs. J Climate 25(6):1827–1846, DOI 10.1175/JCLI-D-11-00227.1, URL https://journals.ametsoc.org/doi/10.1175/JCLI-D-11-00227.1

Buckley MW, Marshall J (2016) Observations, inferences, and mechanisms of the Atlantic Meridional Overturning Circulation: A review. Reviews of Geophysics 54(1):5–63, DOI 10.1002/2015RG000493, URL https://agupubs.onlinelibrary.wiley.com/doi/abs/10.1002/2015RG000493

Cassou C, Kushnir Y, Hawkins E, Pirani A, Kucharski F, Kang IS, Caltabiano N (2018) Decadal Climate Variability and Predictability: Challenges and Opportunities. Bull Amer Meteor Soc 99(3):479–490, DOI 10.1175/BAMS-D-16-0286.1, URL https://journals.ametsoc.org/doi/abs/10.1175/BAMS-D-16-0286.1

Chylek P, Folland CK, Lesins G, Dubey MK, Wang M (2009) Arctic air temperature change amplification and the Atlantic Multidecadal Oscillation. Geophys Res Lett 36(14):L14,801, DOI 10.1029/2009GL038777, URL http://onlinelibrary.wiley.com/doi/10.1029/2009GL038777/abstract

Chylek P, Folland CK, Lesins G, Dubey MK (2010) Twentieth century bipolar seesaw of the Arctic and Antarctic surface air temperatures. Geophysical Research Letters 37(8), DOI 10.1029/2010GL042793, URL https://agupubs.onlinelibrary.wiley.com/doi/full/10.1029/2010GL042793

Clement A, Bellomo K, Murphy LN, Cane MA, Mauritsen T, Rdel G, Stevens B (2015) The Atlantic Multidecadal Oscillation without a role for ocean circulation. Science 350(6258):320–324, DOI 10.1126/science.aab3980, URL http://science.sciencemag.org/content/350/6258/320

Collins M (2002) Climate predictability on interannual to decadal time scales: the initial value problem. Climate Dynamics 19(8):671–692, DOI 10.1007/s00382-002-0254-8, URL https://link.springer.com/article/10.1007/s00382-002-0254-8

Collins M, Allen MR (2002) Assessing the Relative Roles of Initial and Boundary Conditions in Interannual to Decadal Climate Predictability. J Climate 15(21):3104–3109, DOI 10.1175/1520-0442(2002)015⟨3104:ATRROI⟩2.0.CO;2, URL https://journals.ametsoc.org/doi/full/10.1175/1520-0442%282002%29015%3C3104%3AATRROI%3E2.0.CO%3B2

Collins M, Botzet M, Carril AF, Drange H, Jouzeau A, Latif M, Masina S, Otteraa OH, Pohlmann H, Sorteberg A, Sutton R, Terray L (2006) Interannual to Decadal Climate Predictability in the North Atlantic: A Multimodel-Ensemble Study. J Climate 19(7):1195–1203, DOI 10.1175/JCLI3654.1, URL https://journals.ametsoc.org/doi/10.1175/JCLI3654.1

Delworth TL, Mann ME (2000) Observed and simulated multidecadal variability in the Northern Hemisphere. Climate Dynamics 16(9):661–676, DOI 10.1007/s003820000075, URL https://link.springer.com/article/10.1007/s003820000075

Deser C, Phillips AS (2009) Atmospheric Circulation Trends, 1950-2000: The Relative Roles of Sea Surface Temperature Forcing and Direct Atmospheric Radiative Forcing. J Climate 22(2):396–413, DOI 10.1175/2008JCLI2453.1, URL https://journals.ametsoc.org/doi/10.1175/2008JCLI2453.1

Deser C, Magnusdottir G, Saravanan R, Phillips A (2004) The Effects of North Atlantic SST and Sea Ice Anomalies on the Winter Circulation in CCM3. Part II: Direct and Indirect Components of the Response. J Climate 17(5):877–889, DOI 10.1175/1520-0442(2004)017⟨0877:TEONAS⟩2.0.CO;2, URL https://journals.ametsoc.org/doi/10.1175/1520-0442%282004%29017%3C0877%3ATEONAS%3E2.0.CO%3B2

Deser C, Tomas R, Alexander M, Lawrence D (2010) The Seasonal Atmospheric Response to Projected Arctic Sea Ice Loss in the Late Twenty-First Century. J Climate 23(2):333–351, DOI 10.1175/2009JCLI3053.1, URL http://journals.ametsoc.org/doi/full/10.1175/2009JCLI3053.1

Deser C, Tomas RA, Sun L (2015) The Role of Ocean-Atmosphere Coupling in the Zonal-Mean Atmospheric Response to Arctic Sea Ice Loss. J Climate 28(6):2168–2186, DOI 10.1175/JCLI-D-14-00325.1, URL https://journals.ametsoc.org/doi/full/10.1175/JCLI-D-14-00325.1

Deser C, Sun L, Tomas RA, Screen J (2016a) Does ocean coupling matter for the northern extratropical response to projected Arctic sea ice loss? Geophysical Research Letters 43(5):2149–2157, DOI 10.1002/2016GL067792, URL https://agupubs.onlinelibrary.wiley.com/doi/abs/10.1002/2016GL067792

Deser C, Terray L, Phillips AS (2016b) Forced and Internal Components of Winter Air Temperature Trends over North America during the past 50 Years: Mechanisms and Implications. J Climate 29(6):2237–2258, DOI 10.1175/JCLI-D-15-0304.1, URL https://journals.ametsoc.org/doi/abs/10.1175/JCLI-D-15-0304.1

Enfield DB, Mestas-Nuez AM, Trimble PJ (2001) The Atlantic Multidecadal Oscillation and its relation to rainfall and river flows in the continental U.S. Geophysical Research Letters 28(10):2077–2080, DOI 10.1029/2000GL012745, URL https://agupubs.onlinelibrary.wiley.com/doi/abs/10.1029/2000GL012745

Folland CK, Palmer TN, Parker DE (1986) Sahel rainfall and worldwide sea temperatures, 1901-85. Nature 320(6063):602–607, DOI 10.1038/320602a0, URL https://www.nature.com/articles/320602a0

Griffies SM, Bryan K (1997) A predictability study of simulated North Atlantic multidecadal variability. Climate Dynamics 13(7-8):459–487, DOI 10.1007/s003820050177, URL https://link.springer.com/article/10.1007/s003820050177

Gulev SK, Latif M, Keenlyside N, Park W, Koltermann KP (2013) North Atlantic Ocean control on surface heat flux on multidecadal timescales. Nature 499(7459):464–467, DOI 10.1038/nature12268, URL https://www.nature.com/articles/nature12268

Hawkins E, Sutton R (2009) The Potential to Narrow Uncertainty in Regional Climate Predictions. Bull Amer Meteor Soc 90(8):1095–1107, DOI 10.1175/2009BAMS2607.1, URL http://journals.ametsoc.org/doi/abs/10.1175/2009BAMS2607.1

Hawkins E, Sutton R (2011) The potential to narrow uncertainty in projections of regional precipitation change. Clim Dyn 37(1-2):407–418, DOI 10.1007/s00382-010-0810-6, URL https://link.springer.com/article/10.1007/s00382-010-0810-6

He J, Soden BJ (2016a) Does the Lack of Coupling in SST-Forced Atmosphere-Only Models Limit Their Usefulness for Climate Change Studies? J Climate 29(12):4317–4325, DOI 10.1175/JCLI-D-14-00597.1, URL https://journals.ametsoc.org/doi/full/10.1175/JCLI-D-14-00597.1

He J, Soden BJ (2016b) The impact of SST biases on projections of anthropogenic climate change: A greater role for atmosphere-only models? Geophysical Research Letters 43(14):7745–7750, DOI 10.1002/2016GL069803, URL https://agupubs.onlinelibrary.wiley.com/doi/abs/10.1002/2016GL069803

Held IM (2005) The Gap between Simulation and Understanding in Climate Modeling. Bull Amer Meteor Soc 86(11):1609–1614, DOI 10.1175/BAMS-86-11-1609, URL https://journals.ametsoc.org/doi/abs/10.1175/BAMS-86-11-1609

Holland MM, Bitz CM, Tremblay B (2006) Future abrupt reductions in the summer Arctic sea ice. Geophys Res Lett 33(23):L23,503, DOI 10.1029/2006GL028024, URL http://onlinelibrary.wiley.com/doi/10.1029/2006GL028024/abstract

Holton JR (2004) An introduction to dynamic meteorology, 4th edn. International Geophysics Series, Elsevier Academic Press,, Burlington, MA

Hurrell JW, Hack JJ, Shea D, Caron JM, Rosinski J (2008) A New Sea Surface Temperature and Sea Ice Boundary Dataset for the Community Atmosphere Model. J Climate 21(19):5145–5153, DOI 10.1175/2008JCLI2292.1, URL https://journals.ametsoc.org/doi/full/10.1175/2008JCLI2292.1

Kay JE, Deser C, Phillips A, Mai A, Hannay C, Strand G, Arblaster JM, Bates SC, Danabasoglu G, Edwards J, Holland M, Kushner P, Lamarque JF, Lawrence D, Lindsay K, Middleton A, Munoz E, Neale R, Oleson K, Polvani L, Vertenstein M (2015) The Community Earth System Model (CESM) Large Ensemble Project: A Community Resource for Studying Climate Change in the Presence of Internal Climate Variability. Bull Amer Meteor Soc 96(8):1333–1349, DOI 10.1175/BAMS-D-13-00255.1, URL https://journals.ametsoc.org/doi/abs/10.1175/BAMS-D-13-00255.1

Kerr RA (2000) A North Atlantic Climate Pacemaker for the Centuries. Science 288(5473):1984–1985, DOI 10.1126/science.288.5473.1984, URL http://science.sciencemag.org/content/288/5473/1984

Knight JR, Allan RJ, Folland CK, Vellinga M, Mann ME (2005) A signature of persistent natural thermohaline circulation cycles in observed climate. Geophysical Research Letters 32(20), DOI 10.1029/2005GL024233, URL https://agupubs.onlinelibrary.wiley.com/doi/abs/10.1029/2005GL024233

Knight JR, Folland CK, Scaife AA (2006) Climate impacts of the Atlantic Multidecadal Oscillation. Geophysical Research Letters 33(17), DOI 10.1029/2006GL026242, URL https://agupubs.onlinelibrary.wiley.com/doi/abs/10.1029/2006GL026242

Kousky VE, Kagano MT, Cavalcanti IF (1984) A review of the Southern Oscillation: oceanic-atmospheric circulation changes and related rainfall anomalies. Tellus 36:490–504, URL https://onlinelibrary.wiley.com/doi/epdf/10.1111/j.1600-0870.1984.tb00264.x

Li F, Orsolini YJ, Wang H, Gao Y, He S (2018) Atlantic Multidecadal Oscillation Modulates the Impacts of Arctic Sea Ice Decline. Geophysical Research Letters 45(5):2497–2506, DOI 10.1002/2017GL076210, URL https://agupubs.onlinelibrary.wiley.com/doi/abs/10.1002/2017GL076210

Lorenz E (1975) Climatic predictability, the physical basis of climate and climate modelling. GARP Publication Series, Vol. 16, WMO

Lorenz EN (1963) Deterministic Nonperiodic Flow. J Atmos Sci 20(2):130–141, DOI 10.1175/1520-0469(1963)020⟨0130:DNF⟩2.0.CO;2, URL https://journals.ametsoc.org/doi/10.1175/1520-0469%281963%29020%3C0130%3ADNF%3E2.0.CO%3B2

Lu R, Dong B, Ding H (2006) Impact of the Atlantic Multidecadal Oscillation on the Asian summer monsoon. Geophysical Research Letters 33(24), DOI 10.1029/2006GL027655, URL https://agupubs.onlinelibrary.wiley.com/doi/abs/10.1029/2006GL027655

Lyu K, Yu JY, Paek H (2017) The Influences of the Atlantic Multidecadal Oscillation on the Mean Strength of the North Pacific Subtropical High during Boreal Winter. J Climate 30(1):411–426, DOI 10.1175/JCLI-D-16-0525.1, URL https://journals.ametsoc.org/doi/abs/10.1175/JCLI-D-16-0525.1

Meehl GA, Goddard L, Murphy J, Stouffer RJ, Boer G, Danabasoglu G, Dixon K, Giorgetta MA, Greene AM, Hawkins E, Hegerl G, Karoly D, Keenlyside N, Kimoto M, Kirtman B, Navarra A, Pulwarty R, Smith D, Stammer D, Stockdale T (2009) Decadal Prediction: Can it be skillful? Bull Amer Meteor Soc 90(10):1467–1486, DOI 10.1175/2009BAMS2778.1, URL https://journals.ametsoc.org/doi/abs/10.1175/2009BAMS2778.1

Meehl GA, Goddard L, Boer G, Burgman R, Branstator G, Cassou C, Corti S, Danabasoglu G, Doblas-Reyes F, Hawkins E, Karspeck A, Kimoto M, Kumar A, Matei D, Mignot J, Msadek R, Navarra A, Pohlmann H, Rienecker M, Rosati T, Schneider E, Smith D, Sutton R, Teng H, van Oldenborgh GJ, Vecchi G, Yeager S (2014) Decadal Climate Prediction: An Update from the Trenches. Bull Amer Meteor Soc 95(2):243–267, DOI 10.1175/BAMS-D-12-00241.1, URL https://journals.ametsoc.org/doi/abs/10.1175/BAMS-D-12-00241.1

Ménégoz M, Cassou C, Swingedouw D, Ruprich-Robert Y, Bretonnière PA, Doblas-Reyes F (2018) Role of the Atlantic Multidecadal Variability in modulating the climate response to a Pinatubo-like volcanic eruption. Clim Dyn pp 1–21, DOI 10.1007/s00382-017-3986-1, URL https://link.springer.com/article/10.1007/s00382-017-3986-1

Miles MW, Divine DV, Furevik T, Jansen E, Moros M, Ogilvie AEJ (2014) A signal of persistent Atlantic multidecadal variability in Arctic sea ice. Geophys Res Lett 41(2):2013GL058,084, DOI 10.1002/2013GL058084, URL http://onlinelibrary.wiley.com/doi/10.1002/2013GL058084/abstract

Monselesan DP, O'Kane TJ, Risbey JS, Church J (2015) Internal climate memory in observations and models. Geophysical Research Letters 42(4):1232–1242, DOI 10.1002/2014GL062765, URL https://agupubs.onlinelibrary.wiley.com/doi/abs/10.1002/2014GL062765

Msadek R, Dixon KW, Delworth TL, Hurlin W (2010) Assessing the predictability of the Atlantic meridional overturning circulation and associated fingerprints. Geophysical Research Letters 37(19), DOI 10.1029/2010GL044517, URL https://agupubs.onlinelibrary.wiley.com/doi/abs/10.1029/2010GL044517

Murphy LN, Bellomo K, Cane M, Clement A (2017) The role of historical forcings in simulating the observed Atlantic multidecadal oscillation. Geophysical Research Letters 44(5):2472–2480, DOI 10.1002/2016GL071337, URL https://agupubs.onlinelibrary.wiley.com/doi/abs/10.1002/2016GL071337

Neale RB, Richter J, Park S, Lauritzen PH, Vavrus SJ, Rasch PJ, Zhang M (2013) The Mean Climate of the Community Atmosphere Model (CAM4) in Forced SST and Fully Coupled Experiments. J Climate 26(14):5150–5168, DOI 10.1175/JCLI-D-12-00236.1, URL https://journals.ametsoc.org/doi/10.1175/JCLI-D-12-00236.1

Osborne JM, Screen JA, Collins M (2017) Ocean–Atmosphere State Dependence of the Atmospheric Response to Arctic Sea Ice Loss. J Climate 30(5):1537–1552, DOI 10.1175/JCLI-D-16-0531.1, URL http://journals.ametsoc.org/doi/abs/10.1175/JCLI-D-16-0531.1

Palmer TN (2000) Predicting uncertainty in forecasts of weather and climate. Rep Prog Phys 63(2):71, DOI 10.1088/0034-4885/63/2/201, URL http://stacks.iop.org/0034-4885/63/i=2/a=201

Ruprich-Robert Y, Cassou C (2015) Combined influences of seasonal East Atlantic Pattern and North Atlantic Oscillation to excite Atlantic multidecadal variability in a climate model. Clim Dyn 44(1-2):229–253, DOI 10.1007/s00382-014-2176-7, URL https://link.springer.com/article/10.1007/s00382-014-2176-7

Ruprich-Robert Y, Msadek R, Castruccio F, Yeager S, Delworth T, Danabasoglu G (2016) Assessing the Climate Impacts of the Observed Atlantic Multidecadal Variability Using the GFDL CM2.1 and NCAR CESM1 Global Coupled Models. J Climate 30(8):2785–2810, DOI 10.1175/JCLI-D-16-0127.1, URL https://journals.ametsoc.org/doi/full/10.1175/JCLI-D-16-0127.1

Sardeshmukh PD, Hoskins BJ (1985) Vorticity balances in the tropics during the 1982-83 El Niio-Southern oscillation event. Quarterly Journal of the Royal Meteorological Society 111(468):261–278, DOI 10.1002/qj.49711146802, URL https://rmets.onlinelibrary.wiley.com/doi/abs/10.1002/qj.49711146802

Sardeshmukh PD, Hoskins BJ (1988) The Generation of Global Rotational Flow by Steady Idealized Tropical Divergence. J Atmos Sci 45(7):1228–1251, DOI 10.1175/1520-0469(1988)045⟨1228:TGOGRF⟩2.0.CO;2, URL https://journals.ametsoc.org/doi/abs/10.1175/1520-0469(1988)045%3C1228:TGOGRF%3E2.0.CO%3B2

Scaife AA, Smith D (2018) A signal-to-noise paradox in climate science. npj Climate and Atmospheric Science 1(1):28, DOI 10.1038/s41612-018-0038-4, URL https://www.nature.com/articles/s41612-018-0038-4

Schloesser F, Furue R, McCreary JP, Timmermann A (2012) Dynamics of the Atlantic meridional overturning circulation. Part 1: Buoyancy-forced response. Progress in Oceanography 101(1):33–62, DOI 10.1016/j.pocean.2012.01.002, URL http://www.sciencedirect.com/science/article/pii/S0079661112000031

Screen JA (2017) Simulated Atmospheric Response to Regional and Pan-Arctic Sea Ice Loss. J Climate 30(11):3945–3962, DOI 10.1175/JCLI-D-16-0197.1, URL https://journals.ametsoc.org/doi/abs/10.1175/JCLI-D-16-0197.1

Screen JA, Francis JA (2016) Contribution of sea-ice loss to Arctic amplification is regulated by Pacific Ocean decadal variability. Nature Clim Change 6(9):856–860, DOI 10.1038/nclimate3011, URL https://www.nature.com/nclimate/journal/v6/n9/full/nclimate3011.html

Screen JA, Simmonds I (2010) The central role of diminishing sea ice in recent Arctic temperature amplification. Nature 464(7293):1334–1337, DOI 10.1038/nature09051, URL https://www.nature.com/articles/nature09051

Screen JA, Simmonds I, Deser C, Tomas R (2013) The Atmospheric Response to Three Decades of Observed Arctic Sea Ice Loss. J Climate 26(4):1230–1248, DOI 10.1175/JCLI-D-12-00063.1, URL https://journals.ametsoc.org/doi/10.1175/JCLI-D-12-00063.1

Semenov VA, Latif M (2015) Nonlinear winter atmospheric circulation response to Arctic sea ice concentration anomalies for different periods during 1966–2012. Environ Res Lett 10(5):054,020, DOI 10.1088/1748-9326/10/5/054020, URL http://stacks.iop.org/1748-9326/10/i=5/a=054020

Shimizu MH, de Albuquerque Cavalcanti IF (2011) Variability patterns of Rossby wave source. Climate Dynamics 37(3):441–454, DOI 10.1007/s00382-010-0841-z, URL https://doi.org/10.1007/s00382-010-0841-z

Smith DM, Dunstone NJ, Scaife AA, Fiedler EK, Copsey D, Hardiman SC (2017) Atmospheric Response to Arctic and Antarctic Sea Ice: The Importance of OceanAtmosphere Coupling and the Background State. J Climate 30(12):4547–4565, DOI 10.1175/JCLI-D-16-0564.1, URL https://journals.ametsoc.org/doi/abs/10.1175/JCLI-D-16-0564.1

Stocker TF, Coauthors (2013) Climate change 2013: The physical science basis. Cambridge University Press

Sun L, Deser C, Tomas RA (2015) Mechanisms of Stratospheric and Tropospheric Circulation Response to Projected Arctic Sea Ice Loss. J Climate 28(19):7824–7845, DOI 10.1175/JCLI-D-15-0169.1, URL https://journals.ametsoc.org/doi/full/10.1175/JCLI-D-15-0169.1

Sutton RT, Hodson DLR (2005) Atlantic Ocean forcing of North American and European summer climate. Science 309(5731):115–118, DOI 10.1126/science.1109496

Taylor KE (2001) Summarizing multiple aspects of model performance in a single diagram. Journal of Geophysical Research: Atmospheres 106(D7):7183–7192, DOI 10.1029/2000JD900719, URL https://agupubs.onlinelibrary.wiley.com/doi/abs/10.1029/2000JD900719

Taylor KE, Stouffer RJ, Meehl GA (2012) An Overview of CMIP5 and the Experiment Design. Bull Amer Meteor Soc 93(4):485–498, DOI 10.1175/BAMS-D-11-00094.1, URL https://journals.ametsoc.org/doi/10.1175/BAMS-D-11-00094.1

Thompson DWJ, Wallace JM (1998) The Arctic oscillation signature in the wintertime geopotential height and temperature fields. Geophysical Research Letters 25(9):1297–1300, DOI 10.1029/98GL00950, URL https://agupubs.onlinelibrary.wiley.com/doi/abs/10.1029/98GL00950

Trenberth KE, Shea DJ (2006) Atlantic hurricanes and natural variability in 2005. Geophysical Research Letters 33(12), DOI 10.1029/2006GL026894, URL https://agupubs.onlinelibrary.wiley.com/doi/full/10.1029/2006GL026894

UNFCCC (2015) Adoption of the Paris Agreement. URL http://unfccc.int/resource/docs/2015/cop21/eng/l09r01.pdf

Vallis GK (2006) Atmospheric and Oceanic Fluid Dynamics. Cambridge University Press, Cambridge, U.K.

Vial J, Cassou C, Codron C, Bony S, Ruprich-Robert Y (2018) Influence of the Atlantic meridional overturning circulation on the tropical climate response to CO2 forcing: the strong-gets-weaker mechanism, Manuscript submitted for publication

Vihma T (2014) Effects of Arctic Sea Ice Decline on Weather and Climate: A Review. Surv Geophys 35(5):1175–1214, DOI 10.1007/s10712-014-9284-0, URL https://link.springer.com/article/10.1007/s10712-014-9284-0

Voldoire A, Sanchez-Gomez E, Mélia DSy, Decharme B, Cassou C, Sénési S, Valcke S, Beau I, Alias A, Chevallier M, Déqué M, Deshayes J, Douville H, Fernandez E, Madec G, Maisonnave E, Moine MP, Planton S, Saint-Martin D, Szopa S, Tyteca S, Alkama R, Belamari S, Braun A, Coquart L, Chauvin F (2013) The CNRM-CM5.1 global climate model: description and basic evaluation. Clim Dyn 40(9-10):2091–2121, DOI 10.1007/s00382-011-1259-y, URL http://link.springer.com/article/10.1007/s00382-011-1259-y

Watanabe M, Shiogama H, Tatebe H, Hayashi M, Ishii M, Kimoto M (2014) Contribution of natural decadal variability to global warming acceleration and hiatus. Nature Climate Change 4(10):893–897, DOI 10.1038/nclimate2355, URL https://www.nature.com/articles/nclimate2355

Zhang L, Wang C (2013) Multidecadal North Atlantic sea surface temperature and Atlantic meridional overturning circulation variability in CMIP5 historical simulations. Journal of Geophysical Research: Oceans 118(10):5772–5791, DOI 10.1002/jgrc.20390, URL https://agupubs.onlinelibrary.wiley.com/doi/abs/10.1002/jgrc.20390

Zhang R, Delworth TL (2006) Impact of Atlantic multidecadal oscillations on India/Sahel rainfall and Atlantic hurricanes. Geophysical Research Letters 33(17), DOI 10.1029/2006GL026267, URL https://agupubs.onlinelibrary.wiley.com/doi/abs/10.1029/2006GL026267